JOURNAL OF COMPUTATIONAL PHYSICS **144,** 517–549 (1998)
ARTICLE NO. CP986009

Efficient Pseudospectral Flow Simulations in Moderately Complex Geometries

Costas D. Dimitropoulos, Brian J. Edwards,[1] Kyung-Sun Chae,[2] and Antony N. Beris[3]

Department of Chemical Engineering, University of Delaware, Newark, Delaware 19716
E-mail: beris@che.udel.edu

Received July 15, 1997; revised April 21, 1998

A computationally efficient pseudospectral method is developed for incompressible flow simulations in two-dimensional geometries involving periodicity in one direction and significant surface deformations. A pseudoconformal mapping is used to map the flow domain into a rectangle, thereby establishing an orthogonal curvilinear coordinate system within which the governing equations are formulated. The time integration of the spectrally discretized, two-dimensional momentum equations is performed by a second-order mixed explicit/implicit time integration scheme. The satisfaction of the continuity equation is obtained through the solution of a Poisson equation for the pressure and the use of the influence matrix technique. A highly efficient iterative solver has been developed for the solution of a generalized Stokes problem at each time step based on a spectrally preconditioned biconjugate gradient algorithm, which exhibits almost linear scalability, requiring an order $N \log_2 N$ number of operations, where N is the number of unknowns. Numerical results are presented for two-dimensional steady, oscillatory, and peristaltic flows within an undulating channel, which agree well with previous results that have appeared in the literature.

1. INTRODUCTION

Multidimensional and time-dependent flows within an irregular geometry, fixed but also possibly time-dependent, are encountered in many industrial processes (such as, for example, material manufacturing processes) and natural biological systems (such as, for example, blood flow in arteries). Moreover, free surface flows, where one of the fluid boundaries is

[1] Present address: Department of Materials, ETH Zürich, Institute of Polymers, Swiss Federal Institute of Technology Rheocenter, CH-80902, Zürich, Switzerland.

[2] Present address: National Institute of Technology and Quality, 2 Joongang-dong Kwacheon City, Kyunggi-do, 427-010, Korea.

[3] Author to whom all correspondence should be addressed.

0021-9991/98 $25.00

dynamically determined, are additionally important to ocean engineering, naval operations, geosciences, *etc*. The flow problems become even more complicated in the presence of surfactants, the interaction of which with the flow through the modification of the surface tension intimately couples the fluid free surface and surfactant concentration [1, 2]. Therefore, it is not surprising that the solution of these problems can only be achieved (except on rare occasions) numerically. However, the inherent complexity of the governing equations is such that even a numerical solution, using currently available numerical techniques, is, in general, very computationally intensive (indeed, prohibitively so when a fully developed turbulent flow is involved), even when the fluid involved is assumed Newtonian. Thus arises the realization that further progress can only be achieved through the development of new, computationally efficient algorithms. The development of such a new numerical algorithm, based on spectral methods, and its testing with model flow problems with solid boundaries is the subject of the present paper. Its extension to free surface problems with surfactants will be addressed in a subsequent publication.

Among the numerical methods developed for the solution of multi-dimensional and time-dependent Newtonian flow problems, spectral methods are distinguished in that they are both very accurate (converging exponentially fast with mesh refinement) and, based on the availability of Fast Fourier Transforms (FFTs), they have the potential for a very efficient computational implementation (with a workload increasing only mildly faster than linearly, $O(N \log_2 N)$, with the number of modes involved, N) [3, 4]. This combination of high accuracy with computational efficiency has made spectral methods the methods of choice within their domain of application. Indeed, most of the standard turbulence direct numerical simulation data (essentially, homogeneous turbulence [5] and turbulence in a channel flow [6]) have been obtained with spectral approximations.

Roughly, the exponential convergence of spectral approximations is guaranteed for smooth solutions which are, in general, anticipated for flows with smooth geometric boundaries [3, 7]. This places some (but not very severe) restrictions on the utility of spectral methods. However, the other characteristic of the spectral methods, namely their computational efficiency of $O(N \log_2 N)$, relies critically (so far) on the use of fast Poisson solvers. Unfortunately, these are only available for a very limited number of smooth geometries, such as a channel, pipe, or eccentric cylinders geometry, where the coordinate dependencies decouple in the Poisson equation [3]. Thus, with the exception of direct numerical simulation of turbulent flows within simple geometries, current implementations of spectral methods do not perform with $O(N \log_2 N)$ efficiency, which makes their application to large scale flow simulations computationally limited to rather simple flow geometries and/or flow structures. Indeed, for complicated flow geometries, lower order approximation techniques (such as finite difference [8], finite elements [9, 10], and, more recently, finite volume [11, 12]), are in general preferred. Nevertheless, when high accuracy is required (as, for example, in transition and turbulent flow or in free surface flows involving surfactants) the high accuracy spectral approximation becomes almost a necessity for a successful numerical simulation [8]. This has motivated a considerable amount of work for the extension of the applicability of these methods to more complex geometries [13–15].

In order to extend the applicability of spectral methods to the solution of flow problems with irregular boundaries, two approaches have been followed so far. The first involves a mapping of the flow geometry onto a rectangular one, where the spectral approximation can be implemented directly [13]. An application of this approach for two-dimensional pseudospectral flow calculations in an irregular domain with a non-orthogonal coordinate

system can be found in [16]. The second approach involves the use of macro-elements, with respect to which the global geometry is described [14, 15]. The spectral approximation is then used to approximate the variables within each of these elements, whereas lower-order continuity is imposed on the inter-element boundaries. It should be noted that the mapping of the flow boundary into a rectangular domain is also typically used in conjunction with the second approach when the macro-elements have irregular shapes (*e.g.*, spectral elements) [14, 15]. One method of obtaining this mapping is through the solution of a Poisson equation for the new coordinates in terms of the old ones (orthogonal mapping) which is similar to the pseudoconformal mapping discussed in more detail below but does not make use of the special identities that this last one offers.

The major issue that arises with any of the pre-existing spectral techniques is their efficient computational implementation. Although significant strides have been made in that direction, the implementation of either one of the above-mentioned approaches requires the solution of sets of linear equations involving full matrices. Both direct or iterative methods that have been used to achieve that solution have so far failed to demonstrate an optimum $O(N \log_2 N)$ efficiency. It is the purpose of the present work to propose an alternative approach which, by exploiting the special structure of the equations resulting from a pseudoconformal mapping of the original (deformed) domain, allows for the use of specially preconditioned conjugate gradient techniques that, as numerical evidence suggests, seem to lead to an optimum $O(N \log_2 N)$ computational efficiency. This method resulted as the outgrowth of a similar approach proposed for the solution of generalized Helmholtz problems in a previous paper [17].

In general, at the present time, any numerical method developed for the solution of Newtonian flow problems within deformed boundaries involves a step where the computational grid is numerically generated, whether or not the problem has a time dependency and/or a free surface. Fundamental discussions of many grid generation techniques are provided in [18, 19], together with applications to various areas involving the numerical solution of partial differential equations.

Conformal mapping is a strategic method of numerical grid generation which allows for a considerable structure in writing the governing equations in the transformed coordinates for flow problems involving irregular geometric boundaries. This technique takes advantage of the mathematical and computational simplicity of the transformation between the physical and computational domain that occurs when the scale factors are equal to each other. It has the advantage that the partial differential equations expressed in that coordinate system acquire the minimal number of additional terms because the coupling of the two independent variables is limited to only lower-order terms, which allows the use of efficient iterative solution techniques. Furthermore, numerical codes that are very general in their application can be written, with all computations done on a fixed rectangular grid in the transformed computational space regardless of the shape and movement of the physical boundaries [18]. An additional advantage of conformal mapping is that it allows the use of the same efficient routines to solve for the mapping as those which can be used to solve for the viscous term in the flow equations for constant coefficient problems.

Although conformal mappings require the length scales in the different directions to be correlated in order to allow for a constant ratio of scale factors equal to unity, this problem can be easily alleviated by constructing orthogonal mappings in which the ratio of scale factors is not unity, but constant throughout the domain [19]. Since these mappings can be reduced to conformal mappings through a simple rescaling in one direction, they retain most

of the properties of the conformal mappings and are referred to here and in the following as *pseudoconformal mappings*. Here these are exclusively used in favor of the conformal mapping given the flexibility that they offer in their numerical implementation.

Pseudoconformal mapping has a significant problem in that the dual requirements of orthogonality and the constant ratio of the scale factors are too restrictive. Thus, this mapping can only be defined for a specific class of boundary geometries [20]. Although this class is very restrictive as far as three-dimensional geometries are concerned, it is only mildly restrictive for two-dimensional ones. Indeed, it allows for arbitrarily deformed (but smooth) two-dimensional geometries that are periodic in one direction [21], and this is exactly the case where we are limiting the applications discussed in the present work. Moreover, since dependence on a third periodic dimension can also be considered so that most of the properties discussed here are also transferred there with minimal changes, the applicability of the present approach appears to be extendible to at least three-dimensional problems involving surface variations in one of the two periodic dimensions for which several important applications exist.

The other drawback of pseudoconformal mappings, as explained by Thompson *et al.* [18, 19] and Fornberg [22], is that they are usually ill-conditioned in the sense that small changes in the shape of the mapped region can significantly change the position of some boundary points, and that there is little control over the resulting coordinate system; *i.e.*, the point-wise distribution of computational nodes on the boundaries cannot be specified and internal elemental structure cannot be controlled. Ryskin and Leal [23] proposed two different methods for the orthogonal mapping: a strong constraint method that was designed for free-boundary problems in which a distortion function is specified *a priori*, and a weak constraint method that was designed for fixed-domain problems in which the boundary correspondence is prescribed. Kang and Leal [24] proposed a more developed distortion function for the orthogonal mapping. They solved the Laplace equations for the mapping with Dirichlet-type boundary conditions [23, 24]. For the orthogonal mapping, Duraiswami and Prosperetti [25] used the conformal module of the physical domain for the calculation of distortion functions, which was defined as the ratio of the lengths of two adjacent sides of a quadrilateral. However, in these works, by utilizing distortion functions they modify the properties of the mapping which results in the loss of the mathematical simplicity of the resulting equations; this is precisely the feature that we want to exploit here, since it is utilized for the development of efficient conjugate gradient preconditioners. Therefore, the orthogonal mapping with constant conformal module is developed here (pseudoconformal mapping) particularly for the calculation of time-dependent Newtonian flows with a deformed (and in some cases moving) surface. The high accuracy guaranteed by the spectral solution of the mapping equations whenever the boundary conditions that are applied are regular is expected to compensate for the ill conditioning of the problem. Indeed, the numerical evidence of the model flow problems (as presented in the results section) indicates that an exponential convergence to the solution of the flow problem can be obtained provided that one has a sufficiently accurate solution of the mapping equations, which, for isoparametric methods like the one used here, dictates the lowest bound for the error of the scheme. With this in mind, it is natural to consider using a more refined mesh for the mapping than for the flow equations, which is very simple to apply for fully spectral algorithms, in order to have a means of balancing the accuracy of the scheme with the computational cost in a more flexible way. In this paper we did not use such superparametric mappings for the test problems in order to keep things simple and focus on the fundamental concepts behind the algorithm.

Nevertheless, a superparametric approach is recommended for "production" runs associated with relatively large surface deformations. We must also note that a class of problems that are prime candidates to apply a superparametric mapping are free surface flows.

In this work, we have used as a model flow problem the flow of a Newtonian fluid within a sinusoidally undulating channel. This flow is examined under steady and time-dependent (oscillatory flowrate) conditions corresponding to a fixed solid boundary as well as under moving boundary conditions (pulsating flow), which serves especially well as a test case for the applicability of our technique to free surface problems. Many numerical and experimental studies have been undertaken on two-dimensional Newtonian flows with a sinusoidal boundary. Sobey [26] presented numerical solutions of the time-dependent flows through a furrowed channel, for the steady and unsteady cases, using a finite difference method. He also investigated the occurrence of separation in oscillatory flow [27], and observed steady and oscillatory flow in a rectangular channel [28]. Pozrikidis [29] undertook a study for Stokes flow using the boundary integral method. Nishimura *et al.* investigated the flow characteristics in a channel with a symmetric, wavy wall for steady and oscillatory flows through numerical calculations and experiments. The equations expressed in terms of the vorticity and the stream function were solved by the Galerkin finite element method [30–34].

For moving boundary problems, Burns and Parkes [35], as well as Pozrikidis [36], studied the peristaltic motion under the Stokes flow approximations. Peristaltic motion is defined as the propagation of waves along the flexible walls of a channel or tube. Flows driven by peristaltic motion provide an attractive means of sanitary fluid transport and they are often used in industrial processes. Takabatake and Ayukawa [37] studied peristaltic flows in a channel using a finite difference technique including the stream function and the vorticity as the unknowns in the Navier–Stokes equations. They observed the flow in moving coordinates, which travel with the same speed as the waves: the fully developed flow was treated as steady because the configuration of the wall appears to be stationary. Kumar and Naidu [38] studied peristaltic flow in channels with the finite element method and the streamfunction-vorticity formulation. Takabatake *et al.* [39] considered peristaltic flows in tubes using the same method as in [37]. Peristaltic flow of viscoelastic liquids was considered by Boehme and Friedrich [40] in the moving frame under the Stokes flow approximation. Karageorghis and Phillips [41] solved a laminar flow problem in a constricted channel with a conforming Chebyshev collocation method, wherein the flow region is divided into a number of rectangular subdomains and the governing equations are written in terms of the stream function. For the simulation of unsteady, free-surface flows, Ho and Patera [42] presented a Legendre spectral element method based on the use of arbitrary Lagrangian–Eulerian methods for representation of moving boundaries and the use of semi-implicit time-stepping procedures to partially decouple the free-surface evolution and the bulk Navier–Stokes equations.

In this work we solve for two-dimensional flow problems within a sinusoidally undulating channel utilizing a spectral method developed for the numerical simulation of time-dependent Newtonian flows in a general two-dimensional flow geometry with one periodic direction. The approach followed is based on a fully spectral, spatial representation of the variables, a pseudoconformal mapping of the flow domain into a regular rectangle, coupled to a standard semi-implicit (implicit/explicit) time integration of the resulting (upon spatial discretization and the application of an influence matrix technique [43, 44]) ordinary differential equations. The influence matrix technique is especially appropriate for the development of the pressure boundary conditions under the incompressibility constraint [45, 46]. Except for the mapping implementation, the solution technique follows closely

the very successful time-splitting scheme originally proposed by Orszag and Kells [6], followed by Moin and Kim [47] and later by others [48–52] in direct numerical simulation of turbulent flows. The mapping is essential in order to preserve the computational efficiency of the proposed numerical technique, and it can be carried out numerically in a very efficient manner using fast Poisson solvers, since the required equations are separable [3]. However, simply introducing the pseudoconformal mapping is not sufficient to guarantee an efficient spectral solution to the flow problem, since the decomposition of the flow equations at each time step results in nonseparable elliptic equations to which a fast spectral solver is not directly applicable. In order for the implementation of the method discussed in this work to fulfill all of the abovementioned requirements for accuracy and efficiency, the development of an appropriate iterative solver satisfying these requirements is also necessary.

There has been considerable work related to the solution of nonseparable elliptic equations in recent years. The general trend has been to focus on iterative solvers for use in direct numerical simulations of flow problems in complex geometries. After Orszag's influential paper [13], considerable attention has been devoted to the implementation of preconditioned iterative methods. Various iterative methods have been proposed as a basis for spectral algorithms, such as minimal residual methods [53], conjugate gradient methods [13], and multigrid methods [54, 55]. The proposed preconditioners have varied from incomplete LU-factorizations to spectral solutions of similar/related problems. A general overview exists in [3] and a brief summary of more recent papers in [17]. Recently, Hesthaven demonstrated that by using spectral preconditioners it is possible to effectively precondition the advective and diffusive operators [56]. For the purposes of this work, an efficient pseudospectral solver for such equations, which is based on a spectrally preconditioned biconjugate gradient algorithm, has been developed recently by the authors [17] and is implemented here. The implementation of the solver involves the application of the influence matrix method [43, 44] for the satisfaction of the divergence free condition. The influence matrix method is applied within the preconditioner in a manner that does not affect the efficiency of the method, as it is demonstrated in the following sections.

In summary, we have developed a new numerical technique which couples the accuracy and efficiency of spectral methods with the advantages of conformal mapping between the physical and computational domains. The pseudoconformal mapping and its numerical implementation is discussed in Section 2. The numerical algorithm is presented afterwards in Section 3. In order to validate the algorithm, as far as the direct numerical simulation of solid boundary problems is concerned, steady and pulsating flows are investigated in an undulating channel geometry, and peristaltic flow is considered in time-dependent, deforming-boundary geometry in both laboratory and wave frames. The results from this numerical study are presented in Section 4 along with the relevant discussion. This process allows for a systematic increase of the problem difficulty with the ultimate (realizable) goal of developing a highly accurate and equally efficient numerical method for the solution of time-dependent, free-surface flows with surfactants, which is to be discussed in a forthcoming paper. Finally, the conclusions follow in Section 5.

2. PSEUDOCONFORMAL MAPPING WITH PSEUDOSPECTRAL IMPLEMENTATION

The physical domain under consideration involves one periodic direction (x) and one non-periodic (y), with the lower boundary $y = 0$ corresponding for simplicity to a symmetry line. Therefore, the flow domain is defined through the specification of the upper boundary.

This is assumed to be provided through a function $y(x, t)$, which is either known explicitly or implicitly through a relationship between the time-derivatives dx/dt and dy/dt. The first case is treated in Subsections 2.1–2.3 and the second, of relevance to free-surface problems, in Subsection 2.4.

2.1. *Governing Equations for the x, y Coordinates*

An orthogonal mapping from the computational domain, (ξ, η), to the physical domain, (x, y), is obtained by solving two Laplace equations in a rectangular domain, $(0 \to L, 0 \to H)$ for the $x = x(\xi, \eta)$ and $y = y(\xi, \eta)$ coordinates,

$$\nabla^2 x = \frac{1}{h_\xi h_\eta}\left[\frac{\partial}{\partial \xi}\left(\frac{h_\xi}{h_\eta}\frac{\partial x}{\partial \xi}\right) + \frac{\partial}{\partial \eta}\left(\frac{h_\eta}{h_\xi}\frac{\partial x}{\partial \eta}\right)\right] = 0, \tag{1}$$

$$\nabla^2 y = \frac{1}{h_\xi h_\eta}\left[\frac{\partial}{\partial \xi}\left(\frac{h_\xi}{h_\eta}\frac{\partial y}{\partial \xi}\right) + \frac{\partial}{\partial \eta}\left(\frac{h_\eta}{h_\xi}\frac{\partial y}{\partial \eta}\right)\right] = 0, \tag{2}$$

where

$$h_\xi^2 = \left(\frac{\partial x}{\partial \xi}\right)^2 + \left(\frac{\partial y}{\partial \xi}\right)^2 \qquad \text{and} \qquad h_\eta^2 = \left(\frac{\partial x}{\partial \eta}\right)^2 + \left(\frac{\partial y}{\partial \eta}\right)^2 \tag{3}$$

are the scale factors. Numerically, these equations are solved spectrally within a uniform grid along the periodic (ξ-coordinate) direction and a Gauss–Lobatto grid along the non-periodic (η-coordinate) direction,

$$\xi_i = \frac{iL}{N_\xi}, \qquad \eta_j = \frac{H}{2}\left[\cos\left(\frac{j\pi}{N_y}\right) + 1\right] \; (i = 0, 1, \ldots, N_\xi,\ j = 0, 1, \ldots, N_\eta), \tag{4}$$

where L, H are characterictic lengths along the ξ, η-directions, respectively, and N_ξ, N_η are the numbers of nodes in the designated directions.

Equations (1) and (2) are most easily solved numerically when an additional constraint is specified for the conformal module, M, defined as the squared ratio of the scale factors:

$$M = \left(\frac{h_\xi}{h_\eta}\right)^2 = \textit{constant}. \tag{5}$$

Thus the conformal module has a clear geometrical significance: it specifies the ratio of the sides of a small area in the physical plane which is an image of a small rectangle in the computational plane. When the constant in (5) is unity, the mapping is conformal. An orthogonal system with non-unit M is not conformal by definition, but does trivially correspond to a conformal system through a linear transformation of either one of the curvilinear coordinates which incorporates the constant value of the cell aspect ratio [19]. Henceforth, we shall call such a mapping *pseudoconformal*, corresponding through a suitable modification of Eqs. (1), (2) based on the constraint (5) to the following pseudoconformal system of equations

$$M\frac{\partial^2 x}{\partial \xi^2} + \frac{\partial^2 x}{\partial \eta^2} = 0 \qquad \text{and} \qquad M\frac{\partial^2 y}{\partial \xi^2} + \frac{\partial^2 y}{\partial \eta^2} = 0, \tag{6}$$

subject to appropriate boundary conditions. A crucial step allowing for a direct spectral numerical calculation is that the ξ and η variables separate in (6), which makes possible the use of efficient Poisson solvers for the solution of the conformal system.

Two boundary conditions on the top surface are needed in order to find a solution for this elliptic system. One condition comes from the boundary shape and the other condition comes from the orthogonality condition. As mentioned in the Introduction, we illustrate the application of the method to three different Newtonian flows in this paper. The first two, flow in an undulating channel with a constant and time-periodic flow rate, are simpler cases because they involve a stationary boundary. Thus, the mapping is time-independent and may be solved a single time, outside of the main solution algorithm for the flow equations. The other flow (peristaltic), involves time-dependent mapping which must be incorporated into the solution algorithm and determined at each time step. The techniques employed for obtaining the mapping in each case are outlined in the following subsections.

2.2. *Boundary Conditions for a Prescribed Upper Surface*

When the upper surface is specified *a priori* as a given function of x and the time, t,

$$y = f(x, t), \tag{7}$$

such a relationship can be directly used to specify one of the two needed boundary conditions for the upper surface, $\eta = 1$. For example, for a stationary undulating channel,

$$f(x, t) = H_{av}[1 - \alpha \cos(2\pi x/L)], \tag{8}$$

where $H_{av}(=H)$ is the average half-width of an equivalent straight channel and α is the dimensionless amplitude of the undulation. The additional boundary condition is obtained naturally from the orthogonality condition which ensures that the coordinate lines are perpendicular at each node. This orthogonality is guaranteed by the relationship

$$\left(\frac{\partial x}{\partial \xi}\right)\left(\frac{\partial x}{\partial \eta}\right) + \left(\frac{\partial y}{\partial \xi}\right)\left(\frac{\partial y}{\partial \eta}\right) = 0. \tag{9}$$

This relationship in conjunction with Eq. (8) simplifies to a linear condition

$$\frac{\partial x}{\partial \eta} = -\frac{\partial f}{\partial x}\frac{\partial y}{\partial \eta} \qquad \text{at } \eta = 1. \tag{10}$$

Similar conditions could, in general, be specified for the bottom boundary, $\eta = 0$. Alternatively, for simplicity, we can use symmetry conditions there:

$$\frac{\partial x}{\partial \eta} = 0 \qquad \text{and} \qquad y = 0 \text{ at } \eta = 0. \tag{11}$$

The distribution of the coordinates on the top surface is thus unspecified, so that these values are determined by the mapping itself. Periodic conditions are used along the ξ direction, for $x_p \equiv x - \xi$ and y. All problems under consideration in this work involved channel flow with a periodic flow direction, as dictated by the periodic nature of the boundary shape and symmetry conditions at the centerline. However, the approach is general enough to enable the relaxation of these assumptions in a straightforward fashion.

2.3. *Efficient Pseudospectral Solution of the x, y Coordinate Mapping*

Based on the periodicity requirements, the spectral simulation uses a mixed Chebyshev/Fourier spectral approximation: a Fourier series expansion along the periodic direction (x, which is mapped to ξ) is combined with a Chebyshev series expansion along the non-periodic direction (y, mapped to η). This corresponds to any given periodic variable s, $s = x_p(\equiv x - \xi), y$,

$$s(\xi, \eta) = \sum_{j=-N_\xi/2}^{N_\xi/2-1} \sum_{k=0}^{N_\eta} s_{jk} e^{i(j/N_\xi)(2\pi/L_\xi)\xi} T_k\left(\frac{2\eta}{L_\eta} - 1\right), \tag{12}$$

where the s_{jk} are the spectral coefficients, T_k denotes the kth Chebyshev function, and N_ξ, N_η are the number of modes present in the ξ and η directions, respectively, with L_ξ and L_η representing the corresponding length scales. The total number of spectral modes (unknowns) per variable, N_T, is equal to $N_\xi(N_\eta + 1)$. As usual, the transition between the physical and spectral domain can be performed efficiently using fast Fourier transforms (FFTs) requiring $O(N_T \log_2 N_T)$ operations [3].

Given the availability of efficient direct Poisson solvers for Eqs. (6), the major difficulty for the solution of the mapping coordinates x, y arises from the coupling involved in the specifications of the boundary conditions (8), (10) and the nonlinear constraint (5). This is handled in a computationally efficient way according to the following scheme.

Equations (6) are solved iteratively using two nested iteration loops involving an expansion in terms of basis functions $\tilde{x}_i, \tilde{y}_i$ of the form

$$x_p = \sum_{i=1}^{N_\xi} f_i \tilde{x}_i \qquad \text{and} \qquad y = \sum_{i=1}^{N_\xi} g_i \tilde{y}_i. \tag{13}$$

The outer iteration begins by specifying an initial guess for M, after which the equations

$$M\frac{\partial^2 \tilde{x}}{\partial \xi^2} + \frac{\partial^2 \tilde{x}}{\partial \eta^2} = 0 \qquad \text{and} \qquad M\frac{\partial^2 \tilde{y}}{\partial \xi^2} + \frac{\partial^2 \tilde{y}}{\partial \eta^2} = 0, \tag{14}$$

are solved for each one of the basis functions $\tilde{x}_i, \tilde{y}_i$, subject to boundary conditions

$$\frac{\partial \hat{\tilde{x}}_{ik}}{\partial \eta} = 0 \qquad \text{at } \eta = 0 \tag{15}$$

and

$$\frac{\partial \hat{\tilde{x}}_{ik}}{\partial \eta} = \delta_{ik} \qquad \text{at } \eta = 1, \tag{16}$$

for $\hat{\tilde{x}}_{ik}$, where $\hat{\tilde{x}}_{ik}$ represents the kth Fourier transform, and δ_{ik} is the Kronecker delta, and

$$\hat{\tilde{y}}_{ik} = 0 \qquad \text{at } \eta = 0 \tag{17}$$

and

$$\hat{\tilde{y}}_{ik} = \delta_{ik} \qquad \text{at } \eta = 1 \tag{18}$$

for $\hat{\tilde{y}}_{ik}$, where $\hat{\tilde{y}}_{ik}$ represents the kth Fourier transform. Note that with those boundary conditions the physical mapping of the coefficients f_i and g_i appearing in the expressions indicated in Eq. (13) becomes

$$\frac{\partial \hat{x}_{pk}}{\partial \eta} = f_k \qquad \text{and} \qquad \hat{y}_k = g_k. \tag{19}$$

The above statement, in conjunction with the boundary conditions (7) and (10), allows for an efficient iterative algorithm for the specification of f_i and g_i as follows: an initial guess is provided (typically from a previous solution) which is then used in Eq. (13) to evaluate the right-hand sides in Eqs. (7) and (10), which are then used in conjunction with Eq. (19) to provide new values for the coefficients g_k and f_k. The whole process is then repeated until the coefficients do not change within machine accuracy. The converged values of g_k and f_k are then used to evaluate new estimates for M, which then are used to generate new basis functions $\tilde{x}_k$, $\tilde{y}_k$, continuing this outer iteration until M does not change, again within machine accuracy.

Each iteration of the inner loop, as involving only the values of x, y on the boundary, is very fast. In addition, at the initial stages of the outer iteration, convergence needs only to be satisfied partially (given the uncertainty in M) and a criterion equal to 10^{-3} times the previous value in the change in M, ΔM, is adequate. The major workload is associated with the solution of the basis functions and the evaluation of M (of the order $O(N \log_2 N)$), which, however, does not spend too much time since it is found that in the cases investigated in this work, the convergence of the outer loop is very fast, typically requiring no more than 10 to 20 iterations. By using this scheme with the two nested iterations, it was calculated that the mapping subroutine was 25 times more efficient than if a direct linear iteration scheme were used. Finally, we must note that in order to have an adequate mesh resolution, more Fourier than Chebyshev modes are typically required. For example, in order to map a wavy channel where the aspect ratio of its length to its half-width, L/H_{av}, is equal to 3 and for which the dimensionless amplitude of the undulation, α, is 0.45, one requires more than 128 Fourier modes in order to see a decrease of 8 to 10 orders in the magnitude of the spectral coefficients, with increasing wave number along the Fourier direction. The required Chebyshev coefficients are less than 65. This is usually observed when the mapping approaches the limit of becoming singular. Since the singularities appear first on the mapped boundaries, the rate of convergence of the Fourier approximation is more sensitive and starts decreasing before that of the Chebyshev approximation.

Figure 1 illustrates a typical case of mapping from the non-rectangular region to a simple rectangular region for the stationary solid boundary problem. The coordinate lines tend to be more closely spaced near concave segments and more widely spaced near convex segments.

2.4. *Efficient Solution for the Time Derivatives of the Coordinates*

When the location of the upper surface is no longer known *a priori*, but instead boundary conditions are known which constrain the time derivatives of the mapping of the flow boundary, the mapping coordinates $x = x(\xi, \eta, t)$ and $y = y(\xi, \eta, t)$ are solved indirectly through a numerical integration of their time derivatives. This requires evaluation of the time derivatives of x, y which is achieved by using the same nested iteration algorithm as

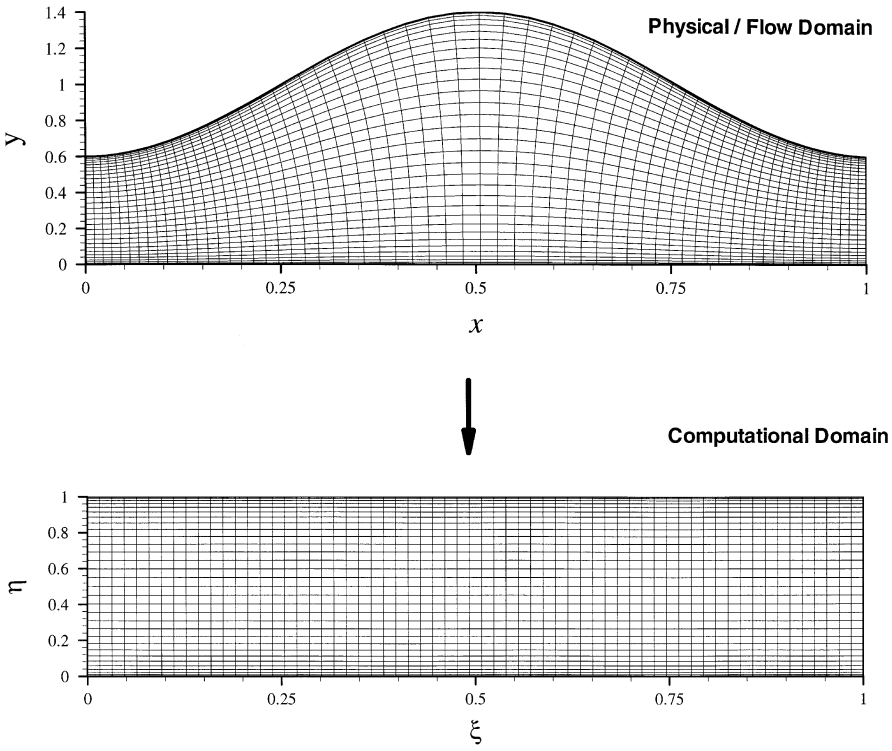

FIG. 1. Mapping of the physical/flow domain to the computational domain.

described for the time-independent mapping. This time, though, one solves the equations

$$M\frac{\partial^2}{\partial\xi^2}\left(\frac{\partial x}{\partial t}\right)+\frac{\partial^2}{\partial\eta^2}\left(\frac{\partial x}{\partial t}\right)=-\frac{\partial M}{\partial t}\frac{\partial^2 x}{\partial\xi^2}$$

and (20)

$$M\frac{\partial^2}{\partial\xi^2}\left(\frac{\partial y}{\partial t}\right)+\frac{\partial^2 y}{\partial\eta^2}\left(\frac{\partial y}{\partial t}\right)=-\frac{\partial M}{\partial t}\frac{\partial^2 y}{\partial\xi^2}$$

for boundary conditions which are derivatives of Eqs. (8) and (10). Specifically, the conditions imposed are

$$\frac{\partial y}{\partial t}=\frac{\partial f(x,t)}{\partial t}\qquad\text{and}\qquad\frac{\partial}{\partial\eta}\left(\frac{\partial x}{\partial t}\right)=-\frac{\partial}{\partial t}\left(\frac{\partial f}{\partial x}\frac{\partial y}{\partial\eta}\right)\text{ at }\eta=1 \tag{21}$$

and

$$\frac{\partial}{\partial\eta}\left(\frac{\partial x}{\partial t}\right)=0\qquad\text{and}\qquad\frac{\partial y}{\partial t}=0\text{ at }\eta=0. \tag{22}$$

The only change compared to the algorithm that calculates the values of the x, y coordinate mapping is that there is an additional iteration loop that corrects for the value of the term $\partial M/\partial t$ which is unknown and must be solved for as well. Also, the right-hand sides in Eqs. (20) are calculated iteratively based on the previous guesses as well. Initial guesses for succeeding time steps are evaluated using first-order continuation.

This approach was tested based on a second order time integration method for the new values of x, y in the case of an undulating channel with a moving wall (at a constant velocity) against the solution of the same problem in a translating frame at the boundary's velocity. In this frame of reference the solid boundary is stationary. The results show differences of the same order as the error of the time integration, which implies that the calculation of the time derivatives has a significantly smaller error.

3. EFFICIENT SPECTRAL NUMERICAL SIMULATION

3.1. *Mathematical Model Equations*

The objective of this paper is to present an efficient spectral numerical method for the solution of time-dependent flows in moderately deformed geometries. We illustrate its application in smoothly deformed channels. Concisely, the method involves the incorporation of a traditional time-splitting implicit/explicit integration of the full Navier–Stokes equation in time, implemented in an orthogonal (pseudoconformal) curvilinear coordinate system and utilizing an efficient elliptic solver to integrate the implicit Poisson/Helmholtz problems which arise at each time step. Thus, the time step solution and computational domain mapping algorithms are closely coupled.

The starting point is the rotational form of the Navier–Stokes equation for incompressible flow and the continuity equation, which in dimensionless form are

$$\frac{\partial \mathbf{v}}{\partial t} + \boldsymbol{\omega} \times \mathbf{v} = -\boldsymbol{\nabla} p + \frac{1}{Re} \nabla^2 \mathbf{v}, \tag{23}$$

$$\boldsymbol{\nabla} \cdot \mathbf{v} = 0, \tag{24}$$

where $\mathbf{v}$ is the dimensionless velocity; p is a dimensionless effective pressure incorporating the kinetic energy contribution $p = \bar{p} + \frac{(\mathbf{v}^2)}{2}$, where $\bar{p}$ is the dimensionless pressure; $\boldsymbol{\omega}$ is the dimensionless vorticity vector field; Re is the Reynolds number, defined as as $Re = UH/\nu$, where ν is the kinematic viscosity of the fluid, and U, H the velocity and length scales. Note that in Eq. (23), p is non-dimensionalized with respect to the inertial scale ρU^2. The velocity scale is different in the three flows presented in this paper and its value will be clarified for each case, as well as the pressure difference, ΔP, between $\xi = 0$ and L, $\Delta L \equiv L$.

The boundary conditions for these equations are as follows. As far as the x-direction is concerned, we have periodic conditions for $\mathbf{v}$ and $p_p \equiv p - \frac{\Delta P}{\Delta L}\xi$:

$$\mathbf{v}|_{\xi=0} = \mathbf{v}|_{\xi=L} \qquad \text{and} \qquad \left.\frac{\partial \mathbf{v}}{\partial \xi}\right|_{\xi=0} = \left.\frac{\partial \mathbf{v}}{\partial \xi}\right|_{\xi=L}, \tag{25}$$

$$p_\rho|_{\xi=0} = p_\rho|_{\xi=L} \qquad \text{and} \qquad \left.\frac{\partial p_\rho}{\partial \xi}\right|_{\xi=0} = \left.\frac{\partial p_\rho}{\partial \xi}\right|_{\xi=L}. \tag{26}$$

For the non-periodic direction y, on the solid surface the velocity boundary conditions are Dirichlet type and are given explicitly as a function $\mathbf{v}_{bnd}$,

$$\mathbf{v} = \mathbf{v}_{bnd} \qquad \text{at } \eta = 1. \tag{27}$$

Their numerical values differ depending on the problem under consideration. Symmetry

conditions are applied along the bottom surface,

$$\frac{\partial v_\xi}{\partial \eta} = 0 \qquad \text{and} \qquad v_\eta = 0 \text{ at } \eta = 0, \tag{28}$$

where v_ξ, v_η are the covariant components of the velocity vector field along the coordinates ξ, η in the computational domain. The pressure in incompressible flows serves as a variable that ensures the satisfaction of the continuity equation and its boundary conditions are imposed through the influence matrix method [43, 44].

Note that for the solution of (23) and (24) in a pseudoconformal curvilinear system, the equations are scaled by nonlinear mapping coefficients which introduce coupling and necessitate the use of iterative solvers to solve the resulting nonseparable elliptic equations at each stage of the integration in time. We have previously worked on developing an efficient and robust iterative spectral solver for nonseparable elliptic equations [17]. This solver was implemented in the integration scheme and will be described in the following sections.

3.2. *Implementation of an Explicit/Implicit Time Integration Scheme in Pseudoconformal Curvilinear Coordinates*

The first step involves the time integration algorithm, where a mixed explicit/implicit method was implemented. It requires taking into consideration the accuracy as well as the stability of each of its components. A fully implicit method would be accuracy rather than stability limited; the associated disadvantages are the necessity of a nonlinear solver and treatment of nonsymmetric and anisotropic matrix operators that typically require memory and work intensive direct solvers [42]. However, in this work we were aiming for an algorithm which exhibits almost linear scalability, $O(N_T \log_2 N_T)$, where N_T is the total number of variables, and we developed it along the lines of previous work on direct numerical simulation of time-dependent Newtonian flows [6, 47–52].

The time integration of Eq. (23) was accomplished by using an Adams–Bashforth second-order explicit method for the nonlinear terms and an Adams–Moulton second-order implicit method for the linear terms. Specifically, after integrating the Navier–Stokes equation,

$$\mathbf{v}^{n+1} - \mathbf{v}^n = -\int_{t_n}^{t_{n+1}} \boldsymbol{\omega} \times \mathbf{v}\, dt - \int_{t_n}^{t_{n+1}} \boldsymbol{\nabla} p\, dt + \int_{t_n}^{t_{n+1}} \frac{1}{Re} \nabla^2 \mathbf{v}\, dt, \tag{29}$$

the following vector equation was obtained

$$\begin{aligned} &(\nabla^2 \mathbf{v})^{n+1} - \frac{2Re}{\Delta t}\mathbf{v}^{n+1} - 2Re\boldsymbol{\nabla}^{n+1} p^{n+1/2} \\ &\quad = -\frac{2Re}{\Delta t}\mathbf{v}^n - (\nabla^2 \mathbf{v})^n - Re\big[(\boldsymbol{\omega} \times \mathbf{v})^{n-1} - 3(\boldsymbol{\omega} \times \mathbf{v})^n\big]. \end{aligned} \tag{30}$$

These equations were evaluated in covariant form in the pseudoconformal curvilinear coordinate system, as described in Appendix A. Each component of Eq. (30) was multiplied by $(h_\xi^2/M)^{n+1}$ in order for it to take the form of a generalized Helmholtz equation, which was solved with the efficient solver presented in [17]. In addition, there exist extra terms in (30) when the mapping is time-dependent. Using various identities for generalized orthogonal

curvilinear coordinate systems, we arrived at the following form for the equations of motion, in covariant components (where substituting ψ with ξ or η produces the ξ or η component of the momentum equation, respectively),

$$\begin{aligned}
&\frac{1}{M^{n+1}}\frac{\partial^2 v_\psi^{n+1}}{\partial \xi^2}+\frac{\partial^2 v_\psi^{n+1}}{\partial \eta^2}-\frac{2Re}{\Delta t}\left(\frac{h_\xi^2}{M}\right)^{n+1} v_\psi^{n+1}-2Re\left(\frac{h_\xi^2}{M}\right)^{n+1}\frac{\partial p^{n+1/2}}{\partial \psi}\\
&\quad=\Lambda(\psi)^{n+1}+\left[v_\psi\left(\frac{1}{M}\frac{\partial^2 \ln h_\xi}{\partial \xi^2}+\frac{\partial^2 \ln h_\xi}{\partial \eta^2}\right)\right]^{n+1}+\left(\frac{h_\xi^2}{M}\right)^{n+1}\left[-\frac{2Re}{\Delta t}\mathbf{v}^n-(\nabla^2\mathbf{v})^n\right]_\psi\\
&\quad\quad-Re\left(\frac{h_\xi^2}{M}\right)^{n+1}[(\boldsymbol{\omega}\times\mathbf{v})^{n-1}-3(\boldsymbol{\omega}\times\mathbf{v})^n]_\psi, \qquad (31)
\end{aligned}$$

where

$$\Lambda(\psi)\equiv\begin{cases}2\left(\frac{\partial v_\xi}{\partial \eta}-\frac{\partial v_\eta}{\partial \xi}\right)\frac{\partial \ln h_\xi}{\partial \eta}, & \psi=\xi\\ -\frac{2}{M}\left(\frac{\partial v_\xi}{\partial \eta}-\frac{\partial v_\eta}{\partial \xi}\right)\frac{\partial \ln h_\xi}{\partial \xi}, & \psi=\eta.\end{cases} \qquad (32)$$

Continuity was imposed indirectly through the solution of a Poisson equation that was obtained by constructing the divergence of $\mathbf{v}^{n+1}$, which was then set to zero, from the components of the time discretized Navier–Stokes equation and multiplying with $(h_\xi^2/M)^{n+1}$. In this way, we took advantage of the pseudoconformal character of the mapping, specifically the constant value of the conformal module M (ratio of the scale factors). The corresponding equation in a compact form is

$$\begin{aligned}
&\frac{1}{M^{n+1}}\frac{\partial^2 p^{n+1/2}}{\partial \xi^2}+\frac{\partial^2 p^{n+1/2}}{\partial \eta^2}\\
&\quad\equiv\left(\frac{h_\xi^2}{M}\right)^{n+1}\{\boldsymbol{\nabla}^{n+1}\cdot(\boldsymbol{\nabla}^{n+1}p^{n+1/2})\}\\
&\quad=\left(\frac{h_\xi^2}{M}\right)^{n+1}\left\{\frac{1}{2Re}\boldsymbol{\nabla}^{n+1}\cdot(\nabla^2\mathbf{v})^{n+1}+\frac{1}{2}\boldsymbol{\nabla}^{n+1}\cdot[(\boldsymbol{\omega}\times\mathbf{v})^{n-1}-3(\boldsymbol{\omega}\times\mathbf{v})^n]\right.\\
&\quad\quad\left.-\frac{1}{2Re}\boldsymbol{\nabla}^{n+1}\cdot\left[-\frac{2Re}{\Delta t}\mathbf{v}^n-(\nabla^2\mathbf{v})^n\right]\right\}. \qquad (33)
\end{aligned}$$

A comprehensive list of the formulae appearing in the above equations can be found in Appendix A.

Equations (31) and (33) had to be solved simultaneously due to the coupling induced through the curvilinear coordinate system. When a solution for the velocities and the pressure was obtained, the values were updated and the time was advanced. Details concerning the application of the iterative biconjugate gradient solver and the imposition of the boundary conditions are discussed in the following sections.

3.3. *Development of an Iterative Spectral Solver for a Set of Nonseparable Stokes-Type Equations*

Equations (31) and (33) can be considered in the following general form during the solution process,

$$\frac{1}{M^{n+1}}\frac{\partial^2 v_\psi^{n+1}}{\partial \xi^2}+\frac{\partial^2 v_\psi^{n+1}}{\partial \eta^2}-\frac{2Re}{\Delta t}\left(\frac{h_\xi^2}{M}\right)^{n+1} v_\psi^{n+1}-2Re\left(\frac{h_\xi^2}{M}\right)^{n+1}\frac{\partial p^{n+1/2}}{\partial \psi}$$
$$=[\mathrm{RHS}(\mathbf{v};\, t=t_{n+1})]_\psi+[\mathrm{RHS}(\mathbf{v};\, t<t_{n+1})]_\psi, \tag{34}$$

$$\frac{1}{M^{n+1}}\frac{\partial^2 p^{n+1/2}}{\partial \xi^2}+\frac{\partial^2 p^{n+1/2}}{\partial \eta^2}=\mathrm{RHS}(p;\, t=t_{n+1})+\mathrm{RHS}(p;\, t<t_{n+1}), \tag{35}$$

where the terms $\mathrm{RHS}(\mathbf{v};\, t=t_{n+1})$, $\mathrm{RHS}(\mathbf{v};\, t<t_{n+1})$, $\mathrm{RHS}(p;\, t=t_{n+1})$, and $\mathrm{RHS}(p;\, t<t_{n+1})$ denote the groups of terms on the right-hand sides of the velocity and pressure equations, calculated before and during the current time step and are defined in Appendix B.

The solver used is the outgrowth of the one that was developed in a previous publication [17] to solve nonseparable elliptic equations re-cast in the form of a modified Helmholtz equation with a non-constant coefficient $g(\xi, \eta)$ in a rectangular domain,

$$\frac{\partial^2 Q}{\partial \xi^2}+R\frac{\partial^2 Q}{\partial \eta^2}-g(\xi,\eta)Q=f(\xi,\eta), \tag{36}$$

where $f(\xi, \eta)$ is an arbitrary function, R a constant, and ξ, η the coordinates of the rectangular computational domain. The solution method developed here consists of a spectrally preconditioned biconjugate gradient algorithm due to Sleijpen and Fokkema [57], which is a generalization of an older algorithm introduced by Van der Vorst [58]. The preconditioner is an iterative algorithm due to Concus and Golub [59], and is applied in conjunction with a fast direct spectral Poisson/Helmholtz equation solver [3] for the repeated solution of a Helmholtz problem with constant coefficients, without it being necessary to reach full convergence (full convergence is not possible with the Concus and Golub algorithm in many cases [17]):

$$\left(\frac{\partial^2}{\partial \xi^2}+R\frac{\partial^2}{\partial \eta^2}-K\right)Q^{i+1}=(g(\xi,\eta)-K)Q^i+f(\xi,\eta). \tag{37}$$

In Eq. (37), the superscript i denotes values at successive iterations and K is a free parameter, which usually has the so-called min-max value:

$$\frac{1}{2}\{\min[g(\xi,\eta)]+\max[g(\xi,\eta)]\}. \tag{38}$$

If desired, the parameter K can be optimized for higher rates of convergence.

This iterative solver exhibited almost linear scalability, requiring approximately $O(N_T \log_2 N_T)$ operations (N_T being the total number of spectral modes), since the most computationally demanding routines are FFTs. Comparing the number of required FFTs with that for a conventional pseudospectral code applied for separable equations where a fast solver can be used, one finds that there exists a larger prefactor, of the order of 10–100,

and thus, it is not as efficient. However, because of the use of an efficient preconditioner, the number of iterations is always of order 10 and therefore, the value of the prefactor never becomes very big. For the problems addressed here, the discretized equations are not separable and a direct solver cannot be used. For small problems it is possible to use a direct solver in association with a conventional pesudospectral method [60–62]. Our experience is that the present code becomes quickly more efficient for meshes larger than 32×33. Spectral element methods can also potentially exhibit $O(N \log_2 N)$ performance, provided that an effective preconditioning of the final equations is available. Unfortunately, even in that case the prefactor is likely to be big as there is no predictable way to achieve a fast convergence. The proposed algorithm, although it does not have the geometric flexibility of methods using domain decomposition, has the advantage of predictable efficiency and high accuracy within its domain of applicability, which is quite broad in its own right.

The proposed algorithm is best suited for use in time-dependent direct numerical simulations, especially when extended to three dimensions, which can be easily accommodated if the third dimension is neutral, *i.e.*, Cartesian (with no mapping) and periodic. In that case, one can still map a domain where the boundaries vary along one of the two periodic dimensions, and use the same principles discussed in [17] to create an algorithm which uses iteratively FFTs and a direct solver for separable elliptic equations. The computational load will be again $O(N_T \log_2 N_T)$ with a relatively small increase in the prefactor compared to the two-dimensional case, since now a few more conjugate gradient iterations are required for convergence of the Stokes-type problem at each time step. However, in three dimensions, the performance of the method is likely that it will overtake that of other implementations not exhibiting almost linear scalability much sooner than in two dimensions due to the much faster increase of the number of unknowns with increasing mesh resolution along each individual direction.

The solution procedure resulting from the extension of this iterative solver to the Stokes-like system of Eqs. (34), (35) consists of the following steps. First, the residuals of Eqs. (34) and (35) are constructed spectrally and are solved iteratively within the preconditioner in the form

$$\left\{ \frac{1}{M^{n+1}} \frac{\partial^2 v_\psi^{n+1}}{\partial \xi^2} + \frac{\partial^2 v_\psi^{n+1}}{\partial \eta^2} - \frac{2Re}{\Delta t} \left(\frac{k}{M} \right)^{n+1} v_\psi^{n+1} - 2Re \left(\frac{k}{M} \right)^{n+1} \frac{\partial p^{n+1/2}}{\partial \psi} \right\}^{i+1}$$

$$= \left\{ \frac{2Re}{\Delta t} \left(\frac{h_\xi^2}{M} - k \right)^{n+1} v_\psi^{n+1} + 2Re \left(\frac{h_\xi^2}{M} - k \right)^{n+1} \frac{\partial p^{n+1/2}}{\partial \psi} \right.$$

$$\left. + [\mathrm{RHS}(\mathbf{v};\, t = t_{n+1})]_\psi + [\mathrm{RHS}(\mathbf{v};\, t < t_{n+1})]_\psi \right\}^{i}, \tag{39}$$

$$\left\{ \frac{1}{M^{n+1}} \frac{\partial^2 p^{n+1/2}}{\partial \xi^2} + \frac{\partial^2 p^{n+1/2}}{\partial \eta^2} \right\}^{i+1} = \{\mathrm{RHS}(p;\, t = t_{n+1}) + \mathrm{RHS}(p;\, t < t_{n+1})\}^{i}, \tag{40}$$

where the superscript i denotes the iteration number to which the values of the variables used to calculate the various terms correspond, and $k = \frac{1}{2}[\min(h_\xi^2) + \max(h_\xi^2)]$. As before [17], this iterative procedure is only carried out for a limited number of iterations (typically 2–4), and the iterative process does not even need to converge for the preconditioner to work efficiently.

The boundary conditions for the pressure were imposed through the influence matrix technique [43, 44]. According to this technique, the pressure boundary conditions are imposed implicitly through the requirement that the divergence of the velocity field at the $n+1$ time step be zero on the boundaries. This was a necessary and sufficient condition, arising naturally from the construction of the divergence of Eq. (30) (and post-multiplication with $(h_\xi^2/M)^{n+1}$) and the substitution of Eq. (33). The equation obtained is

$$\frac{1}{M^{n+1}}\frac{\partial^2}{\partial\xi^2}\left(\frac{h_\xi^2}{M}\nabla\cdot\mathbf{v}\right)^{n+1}+\frac{\partial^2}{\partial\eta^2}\left(\frac{h_\xi^2}{M}\nabla\cdot\mathbf{v}\right)^{n+1}-\frac{2Re}{\Delta t}\left(\frac{h_\xi^2}{M}\nabla\cdot\mathbf{v}\right)^{n+1}=0. \quad (41)$$

One notices immediately that the solution of this Helmholtz equation is zero if and only if the divergence of the velocity is zero on the boundary.

In order to apply the influence matrix technique efficiently, it was used within the preconditioner. In fact, one of the advantages of the chosen preconditioner that led to its selection (apart from the efficiency and accuracy of the resulting iterative solver), was that it can accommodate an efficient application of the influence matrix technique. Specifically, due to the coupling of the Fourier modes arising from the non-constant coefficient of the Helmholtz equations arising from (31), it would be necessary to apply this technique N_ξ times (the number of Fourier modes) and solve an $N_\xi \times N_\xi$ linear system to find the correct coefficients that mandate the pressure boundary conditions. However, a careful look at Eq. (37) revealed that when one performs the transformation described (which is essentially a linearization) to Eqs. (31) and (33), leading to (39) and (40), the resulting equations have constant coefficients and the Fourier modes are decoupled. Therefore, one could proceed in applying the influence matrix technique as in the case where the model equations were separable and fast direct spectral solvers for Helmholtz equations were utilized [51].

3.3.1. *Moving Solid Boundary: Time-Dependent Mapping.* To accommodate a time-dependent mapping, the momentum equations had to be modified with some correcting terms which correspond to the change in time of the covariant basis vectors of the generalized orthogonal curvilinear system used for the mapping between the physical and computational domains. When such a case is considered, which would arise for example for free-surface flows or peristaltic flows when viewed in the laboratory (observer) frame, the proposed algorithm can adapt to the new demands efficiently using the time derivatives calculated in Subsection 2.4. The momentum equations now have some additional terms which are treated as nonlinear, through an Adams–Bashforth integration scheme. The major advantage of the proposed method is that by allowing the mapping of the surface deforming in time to be efficiently evaluated using the same Poisson solvers as with the mapping for a stationary surface and by incorporating explicitly the additional terms into the flow equations at every time step, a computationally efficient and highly accurate numerical simulation of moving boundary problems can be developed. The relevant set of equations in this case becomes

$$\begin{aligned}&\frac{1}{M^{n+1}}\frac{\partial^2 v_\psi^{n+1}}{\partial\xi^2}+\frac{\partial^2 v_\psi^{n+1}}{\partial\eta^2}-\frac{2Re}{\Delta t}\left(\frac{h_\xi^2}{M}\right)^{n+1}v_\psi^{n+1}-2Re\left(\frac{h_\xi^2}{M}\right)^{n+1}\frac{\partial p^{n+1/2}}{\partial\psi}\\&\quad=\Lambda(\psi)^{n+1}+\left[v_\psi\left(\frac{1}{M}\frac{\partial^2\ln h_\xi}{\partial\xi^2}+\frac{\partial^2\ln h_\xi}{\partial\eta^2}\right)\right]^{n+1}+\left(\frac{h_\xi^2}{M}\right)^{n+1}\left[-\frac{2Re}{\Delta t}\mathbf{v}^n-(\nabla^2\mathbf{v})^n\right]_\psi\\&\qquad-Re\left(\frac{h_\xi^2}{M}\right)^{n+1}[(\mathbf{b}+\boldsymbol{\omega}\times\mathbf{v})^{n-1}-3(\mathbf{b}+\boldsymbol{\omega}\times\mathbf{v})^n]_\psi, \quad (42)\end{aligned}$$

where $\psi = \xi, \eta$, $\mathbf{\Lambda}(\psi)$ has been defiend in Eq. (32), and

$$\frac{1}{M^{n+1}}\frac{\partial^2 p^{n+1/2}}{\partial \xi^2} + \frac{\partial^2 p^{n+1/2}}{\partial \eta^2} = \frac{1}{2Re}\left(\frac{1}{h_\xi^2}\right)^{n+1}\left(\frac{1}{M}\frac{\partial^2 \ln h_\xi}{\partial \xi^2} + \frac{\partial^2 \ln h_\xi}{\partial \eta^2}\right)^{n+1}$$
$$\times\left[2\left(v_\xi\frac{\partial \ln h_\xi}{\partial \xi} + Mv_\eta\frac{\partial \ln h_\xi}{\partial \eta}\right) - \frac{v_\xi}{M} - v_\eta\right]^{n+1}$$
$$+\left(\frac{h_\xi^2}{M}\right)^{n+1}\left\{\frac{1}{2}\boldsymbol{\nabla}^{n+1}\cdot[(\mathbf{b}+\boldsymbol{\omega}\times\mathbf{v})^{n-1} - 3(\mathbf{b}+\boldsymbol{\omega}\times\mathbf{v})^n]\right.$$
$$\left.-\frac{1}{2Re}\boldsymbol{\nabla}^{n+1}\cdot\left[-\frac{2Re}{\Delta t}\mathbf{v}^n - (\nabla^2\mathbf{v})^n\right]\right\}, \tag{43}$$

where **b** corresponds to the vector respesenting the additional terms whose covariant components are

$$b_i = \left[\frac{\partial v_i}{\partial u^j} - v_k\Gamma_{ij}^k\right]\frac{du^j}{dt} - v_k\mathbf{g}^k\cdot\left.\frac{\partial \mathbf{g}_i}{\partial t}\right|_{u^j}, \tag{44}$$

where i, j, k are dummy indices corresponding to the coordinates ξ and η, $\mathbf{g}_i$ and $\mathbf{g}^k$ are the covariant and contravariant basis vectors, respectively, and Γ_{ij}^k represents a Christoffel symbol for the curvilinear coordinate system (see Appendix A for detailed expressions).

3.4. *Alternative Formulation Using the Divergence-Free Condition Explicitly*

An alternate route of applying the incompressibility constraint in the equations was also examined. In this procedure, the divergence of the velocity field is imposed as one of the equations to be solved instead of the pressure equation. The implication of this change is that within the preconditioner, where the influence matrix technique is applied, the equation for the pressure is formed directly from the preconditioner velocity equations. The equations for the velocity are the same as (34), whereas the pressure equation becomes

$$\frac{1}{M^{n+1}}\frac{\partial^2 p^{n+1/2}}{\partial \xi^2} + \frac{\partial^2 p^{n+1/2}}{\partial \eta^2} = \frac{1}{2ReM}\frac{\partial}{\partial \xi}\left\{\left(\frac{1}{h_\xi^2}\right)^{n+1}\frac{\partial^2 v_\xi^{n+1}}{\partial \xi^2} + \left(\frac{M}{h_\xi^2}\right)^{n+1}\frac{\partial^2 v_\xi^{n+1}}{\partial \eta^2}\right.$$
$$-\frac{2Re}{\Delta t}v_\xi^{n+1} - \frac{2Re}{\Delta t}\left(\frac{M}{h_\xi^2}\right)^{n+1}[\mathrm{RHS}(\mathbf{v}; t = t_{n+1})]_\xi$$
$$\left.-\frac{2Re}{\Delta t}\left(\frac{M}{h_\xi^2}\right)^{n+1}[\mathrm{RHS}(\mathbf{v}; t < t_{n+1})]_\xi\right\}$$
$$+\frac{1}{2Re}\frac{\partial}{\partial \eta}\left\{\left(\frac{1}{h_\xi^2}\right)^{n+1}\frac{\partial^2 v_\eta^{n+1}}{\partial \xi^2} + \left(\frac{M}{h_\xi^2}\right)^{n+1}\frac{\partial^2 v_\eta^{n+1}}{\partial \eta^2}\right.$$
$$-\frac{2Re}{\Delta t}v_\eta^{n+1} - \frac{2Re}{\Delta t}\left(\frac{M}{h_\xi^2}\right)^{n+1}[\mathrm{RHS}(\mathbf{v}; t = t_{n+1})]_\eta$$
$$\left.-\frac{2Re}{\Delta t}\left(\frac{M}{h_\xi^2}\right)^{n+1}[\mathrm{RHS}(\mathbf{v}; t < t_{n+1})]_\eta\right\}. \tag{45}$$

This formulation was found to result in behavior akin to the simulation method discussed in the previous sections, but it required a larger number of iterations to converge for each time step than the previous, pressure equation formulation. As a result, the pressure equation formulation was utilized in all the applications discussed in the results section below.

4. NUMERICAL RESULTS

The numerical scheme was validated by implementing it in various flow problems examined in the literature and reproducing their results. We examined three different problems, the problem of flow in an undulating channel where a steady state is attained, the problem of oscillatory flow in an undulating channel, and finally peristaltic flow, where the sinusoidal boundary can be considered to be translating with constant velocity along the flow direction x. By comparing the results with those in the literature, we demonstrate the validity and accuracy of our approach.

4.1. *Steady Flow in an Undulating Channel*

We performed simulations of flow in an undulating channel, where we integrated the equations in time to reach some of the steady state solutions reported by Nishimura and co-workers [30–32], who used a finite element method and the streamfunction-vorticity formulation for the flow equations. We implemented the algorithm where the volumetric flowrate Q was specified. The algorithm can be also implemented for a specified pressure drop across the channel as the driving force. The boundary conditions for the velocity at the stationary top boundary are non-slip. Thus, we have two Dirichlet conditions where the velocity components are required to vanish. The Reynolds number in our simulations is defined as $Re \equiv Q/\nu$, where the flowrate is given by the relation $Q = H_{av}u_{av}$, with u_{av} being the average velocity defined by the imposed flowrate and the length scale, which is equal to the average channel half-width H_{av}, taken as unity. The Reynolds number in our work is equal to half the value of that in the work by Nishimura *et al.* [30], which we denote with Re_{NS}. We performed calculations up to $Re = 150$, which corresponds to $Re_{NS} = 300$, and is very close to the region where the flow has a transition to turbulence due to unsteady vortex motion, and where three-dimensional simulation is required ($Re_{NS} = 350$). The amplitude of the undulation of the channel α is equal to $7/13$ and the dimensionless channel length L is $56/13$. As far as the resolution of the simulations is concerned, we used three different meshes. Initially the simulations were carried out with a mesh consisting of 80 Fourier and 33 Chebyshev modes; we repeated with a 64×65 mesh and finally used a 128×65 mesh. The time step used was 5×10^{-4} dimensionless units.

In Table I, we list the calculated values of the friction factor f, defined as $f = H_{av}\Delta P/L$, where $\Delta P/L$ is a dimensionless pressure drop per unit length (scaled in inertial units). Since $H_{av} = 1$, f is equal to $\Delta P/L$. We obtained values of the friction factor for $Re = 0.5$, 10, 50, 150. The values for the most refined mesh are plotted in a logarithmic plot in Fig. 2 to facilitate a comparison with Fig. 7 in [30]. It can be seen that there is quantitative agreement and that the main characteristic, which is a change in the slope around $Re_{NS} = 15$, is captured. As a side note, we should mention that the flowrates corresponding to inertialess flow with various amplitudes of undulation were found in complete agreement with those resulting from very accurate pseudospectral calculations [62], up to all five significant digits reported in that work.

TABLE I
Calculated Friction Factors, f, at Various Reynolds Numbers and Mesh Sizes for Steady Flow in an Undulating Channel

	Calculated friction factor f Mesh size		
Re	80 × 33	64 × 65	128 × 65
0.5	19.394439	19.394440	19.394440
10	1.060200	1.060065	1.060062
50	0.290946	0.290945	0.290943
150	0.116150	0.117656	0.117623

Note. The amplitude of undulation α is $7/13$ and $L/H_{av} = 56/13$.

In Fig. 3, we show the calculated wall vorticity profiles at various Reynolds numbers ($Re = 10, 50, 150$). We have also included the profiles from the simulations in the literature [30]. A comparison is rather favorable since we can see that there is quantitative agreement. There are some differences for the high Reynolds number data. In addition, in all cases the peak of the vorticity is calculated to be located a little before the end of the channel, whereas for the data from [30] it is shown to be at the end of the channel. By observing Fig. 10 in [30], it can also be seen that the experimental value of the vorticity at the end of channel is also slightly less than their predictions. This is also inferred from the results in [31], where they have captured the peak of the wall vorticity before the end of the channel for oscillatory flow (Figs. 5–8 in [31]), and also measured it in experiments (Fig. 8 in [31]).

Finally, for steady flow in an undulating channel we have also performed simulations for a high Reynolds number case and another with high surface deformation in order to provide a better picture of the capabilities of the method. For these simulations, we imposed an external pressure drop, equal to $\Delta P/\Delta L = -1/Re$, to drive the flow. In the first case

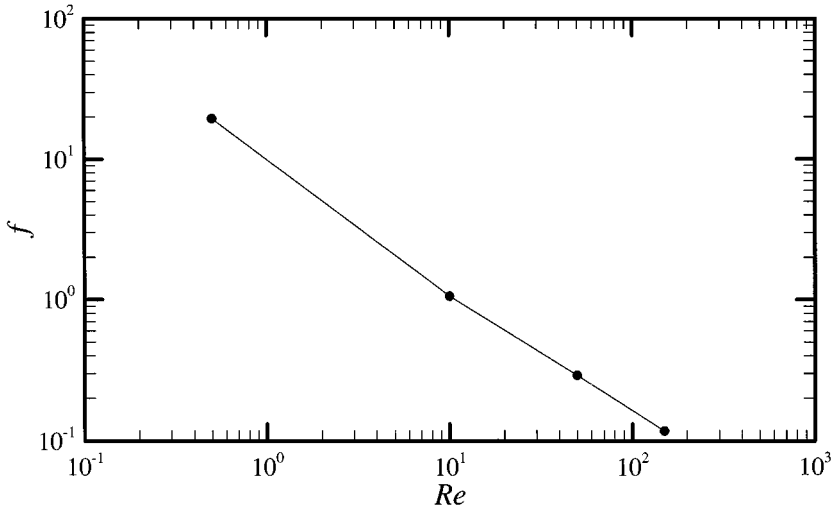

FIG. 2. Calculated friction factor, f, at various Reynolds numbers for steady flow in an undulating channel. The amplitude of undulation, α, is $7/13$, $L/H_{av} = 56/13$, and the mesh size is 128×129.

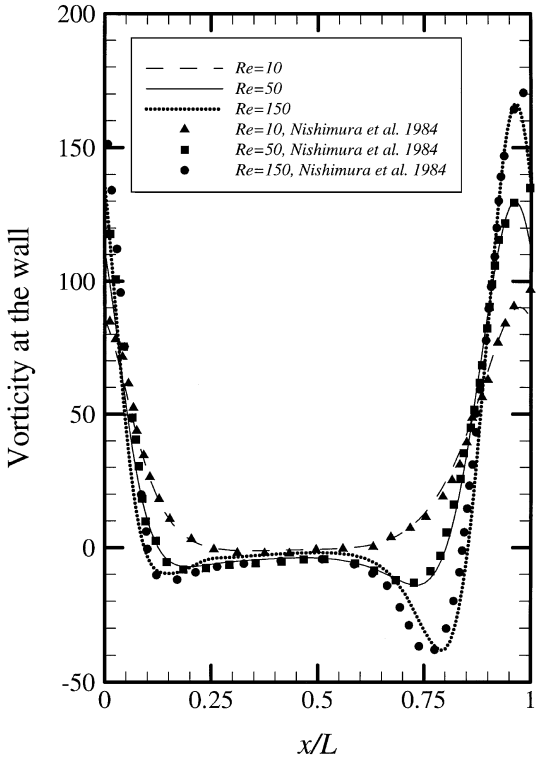

FIG. 3. Calculated wall vorticity profiles at various Reynolds numbers for steady flow in an undulating channel. The amplitude of undulation, α, is $7/13$ and $L/H_{av} = 56/13$. The flow is from left to right.

the amplitude of the undulation of the channel α is 0.15, the dimensionless channel length L/H_{av} is 6.25, the Reynolds number Re is 1000, and the time step is equal to 10^{-3}. Here, we are able to capture the flowfield for a mesh as small as to 32×33 due to the small deformation. Results with a more refined mesh (64×65) showed no changes other than in the truncation error (the calculated flowrate is equal to 0.27390523). This is due to the fact that the mesh is resolved extremely well and the spectral coefficients decay very rapidly to zero for this small deformation, making the small mesh more than sufficient. The magnitudes of $2/3$ of the Fourier modes corresponding to the first Chebyshev mode for the velocity and the x-coordinate of the mesh are plotted in Fig. 4, where one can verify the exponential convergence of the method.

In the second case, $\alpha = 0.45$, $L/H_{av} = 3$, $Re = 10$, $\Delta t = 10^{-3}$, a more refined mesh was necessary due to the large deformation. Simulations with meshes of 64×65, 128×129, and 256×65 revealed that 65 Chebyshev and at least 128 Fourier modes are required for an accurate solution of the mapping which results in a solution accurate to 7 decimal places for the flowrate (see Table II). Figure 5 shows the magnitudes of the Fourier coefficients for this case. One notices the larger number of modes needed to achieve values of the coefficients smaller than 10^{-10} for the mapping coordinates, in contrast to what is necessary for the velocity components. We should emphasize that these two cases demonstrate that the method described in this work can accommodate high Reynolds flows with smaller meshes than flows with high surface deformations, and thus, there is a strong motivation for the use of superparametric mapping. In this way, a relatively large number of spectral modes can be

TABLE II
Calculated Flowrate for Various Meshes for Steady Flow in an Undulating Channel

Mesh size	Flowrate
64 × 65	0.13131848
128 × 129	0.13131907
256 × 65	0.13131904

Note. The amplitude of undulation, α, is 0.15, $L/H_{av} = 3$, and $Re = 10$.

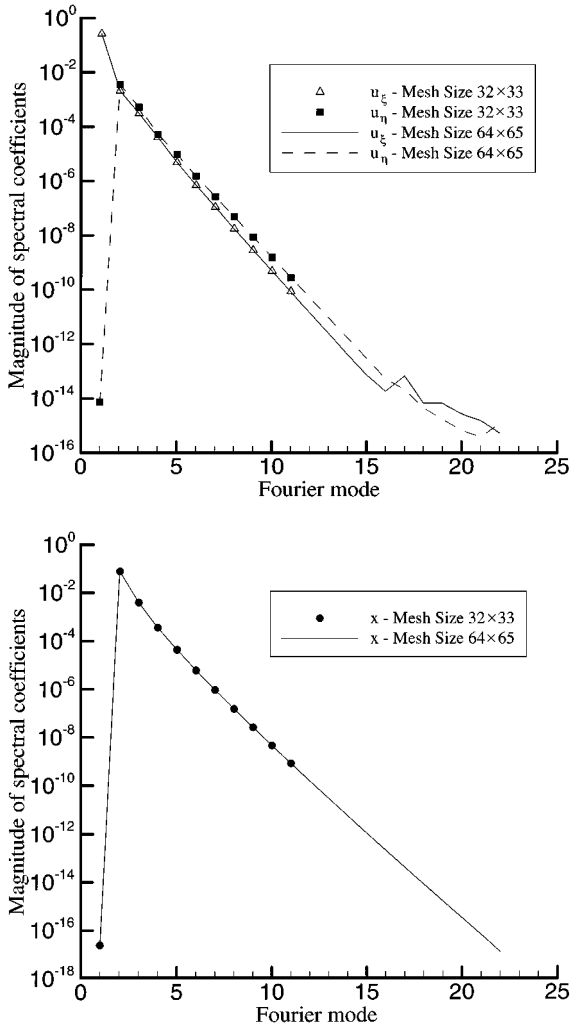

FIG. 4. Steady flow in an undulating channel. Magnitudes of 2/3 of the Fourier modes corresponding to the first Chebyshev mode for the velocity components (a) and the x-coordinate of the mapping (b) at different mesh sizes. $Re = 1000$, the amplitude of undulation, α, is 0.15 and $L/H_{av} = 6.25$.

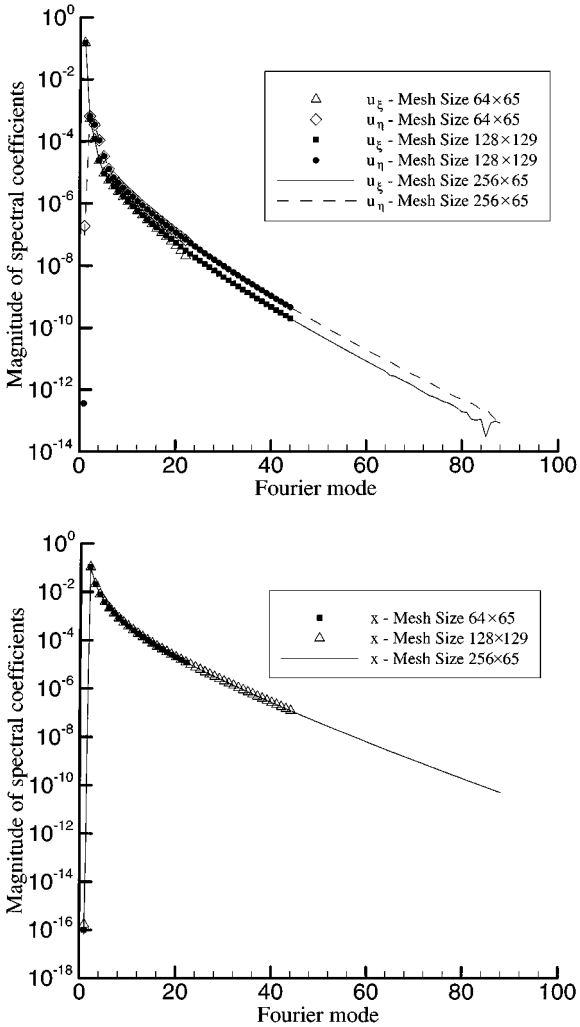

FIG. 5. Steady flow in an undulating channel. Magnitudes of 2/3 of the Fourier modes corresponding to the first Chebyshev mode for the velocity components (a) and the x-coordinate of the mapping (b) at different mesh sizes. $Re = 10$, the amplitude of undulation, α, is 0.45, and $L/H_{av} = 3$.

used only for the mapping problem, making the solution of the flow problem still possible without the use of an excessively large mesh. This is especially important for free-surface flows and three dimensional calculations, where the computational cost associated with the solution of the flow problem is of major significance.

4.2. *Oscillatory Flow in an Undulating Channel*

The method was also implemented for oscillatory flow in an undulating channel, where we were imposing a sinusoidally varying flowrate. In this way we can validate the method in problems where there exists a transient driving force, leading to a stationary rather than a steady state. Our benchmark problem was taken from a paper by Nishimura *et al.* [34]. The geometry of the undulating channel is the same as in the steady flow problem examined previously. The characteristic parameters defining the flow are the Reynolds number

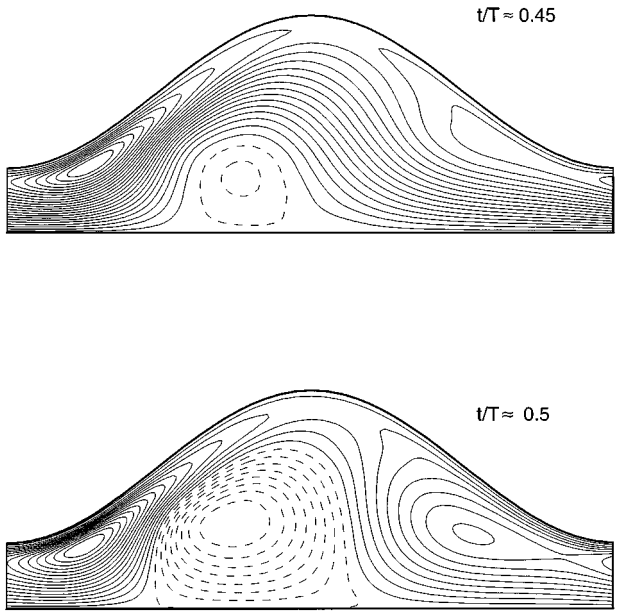

FIG. 6. Oscillatory flow in an undulating channel. Streamline patterns for $Re = 250$ and $St = 0.034$ at two different times, $t/T \approx 0.45$ and 0.5. The amplitude of undulation, α, is 7/13, $L/H_{av} = 56/13$, and the mesh size is 32×17 modes. The flow is from left to right. Dashed lines denote negative contour values.

and the Strouhal number. The Strouhal number is defined as $St = f H_{av}^2 (1-\alpha)^2 / 2Q_{max}$, where f is the frequency of oscillation, H_{av} the average half-width of the channel, α the amplitude of the undulation, and Q_{max} is the maximum flowrate. The Reynolds number is defined as $Re = Q_{max}/\nu$. Finally, the flowrate depends on time through the relationship $Q(t) = Q_{max} \sin(2\pi f t)$. With these definitions, our values for St and Re coincide with those in [34].

Our test case corresponds to $St = 0.034$ and $Re = 250$. Since in [34], streamfunction plots were mainly used with no data for specific values of the streamlines, for a series of runs we focused on a less quantitative level than in the steady flow case and used a coarser mesh (32 Fourier modes by 17 Chebyshev modes). The time step Δt was 5×10^{-4} dimensionless units. With this resolution we could integrate the equations in time until we reached the stationary state observed in such flows faster, but we also retained enough accuracy to capture the characteristics of the flow field. As can be seen from Fig. 6, where we have two plots of the streamlines at different times, the flow-field starts separating into three distinct regions until a maximum separation is reached. These two snapshots agree well with the corresponding plots in Fig. 2 from [34]. Figure 7 shows mesh convergence of the algorithm for a finer mesh 128×65 and the same time step as before, from another series of runs. We present a succession of contour plots at different times, where we have noted the values for the streamfunction. The results for $t/T = 0.5$ coincide with the results in the literature [34].

4.3. *Examination of Peristaltic Flow in Two Reference Frames*

The most interesting benchmark problem for us was the examination of peristaltic flow. Peristaltic flow arises from the propagation along the length of the channel of a progressive wave, resulting from the contraction and expansion of an extensible boundary of the channel.

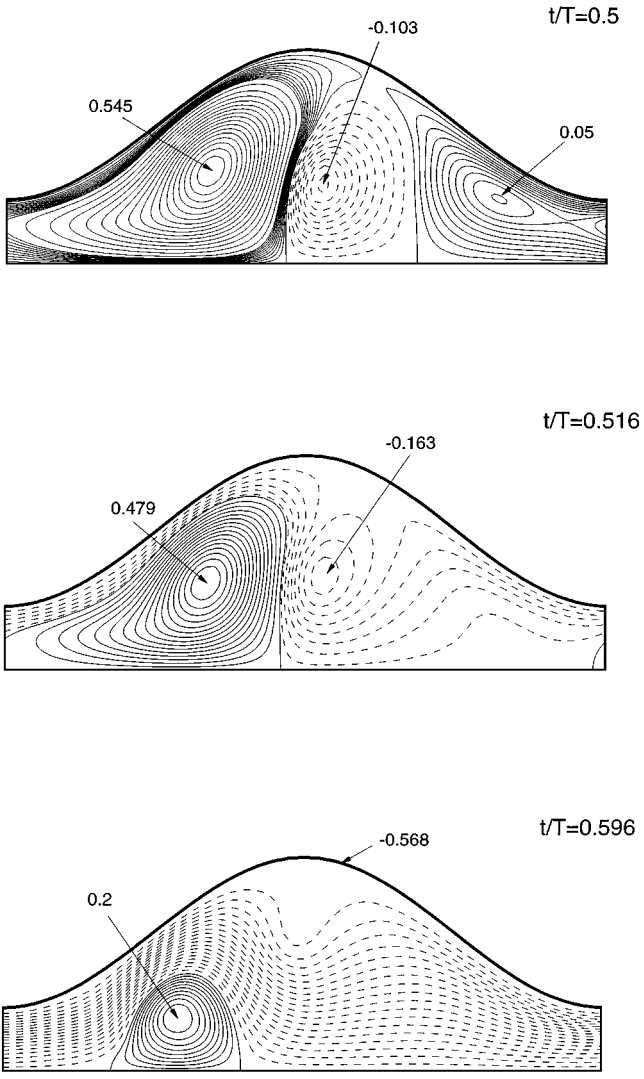

FIG. 7. Oscillatory flow in an undulating channel. Streamline patterns for $Re = 250$ and $St = 0.034$ at three different times, $t/T = 0.5$, 0.516, and 0.596. The amplitude of undulation, α, is $7/13$, $L/H_{av} = 56/13$, and the mesh size is 128×65 modes. The flow is from left to right. Dashed lines denote negative contour values.

Such flows are abundant in the human body, where the phenomenon of peristalsis drives the mixing and transport of fluids. In addition, peristaltic pumping of fluids, which is a means of sanitary transport (since there is no contact of fluid with mechanical parts of the pump), has been utilized in diverse applications ranging from biomedical (*i.e.*, circulation of blood within artificial organs) to classical chemical industry processes, like the transport of slurries and corrosives [37]. In addition to the significance of such applications, peristaltic flow from a numerical standpoint provides us the opportunity to test our method for unsteady flows, when we formulate the problem in the laboratory (observer frame). In addition, we can use only the time-dependent mapping solution, assuming that we do not know the location of the surface *a priori*, which leaves us with a problem very close to what we will have when considering time-dependent free-surface flows with this numerical scheme.

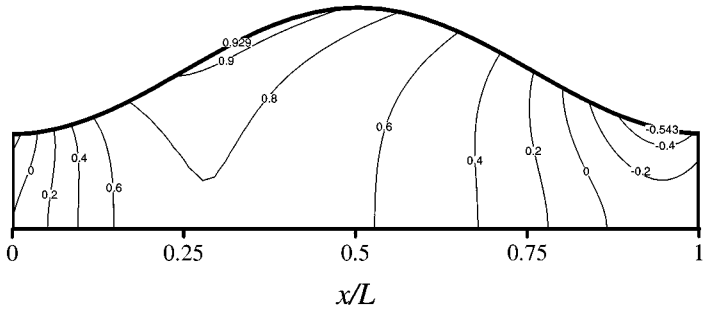

FIG. 8. Pressure contours $Re = 5$, $\alpha = 0.4$, $L/H_{av} = 5$, and $\Delta P/\Delta L = 0$ in peristaltic flow calculated in the wave frame. The peristaltic wall (upper boundary) moves from left to right.

Specifically, we considered as before a two-dimensional channel with a moving sinusoidal top boundary. This so-called peristaltic wall of the channel is defined by the following equation for its height h,

$$h(x,t) = H_{av}\left\{1 - \alpha\cos\left[\frac{2\pi}{L}(x - ct)\right]\right\}, \tag{46}$$

where H_{av} is the average half-width of the channel, α is the dimensionless amplitude of the undulation, L is the channel's length, and c is the velocity of propagation. At $y = 0$ we imposed again symmetry conditions.

This problem can be considered steady when formulated in a frame moving with constant velocity c (wave frame) through a Gallilean transformation. In the wave frame, the peristaltic boundary is stationary and the top boundary is given by Eq. (8), and the only thing that changes are the velocity boundary conditions. In fact, all studies so far have been done in the wave frame. In the wave frame we solved a problem from [37] to test the method for non-zero boundary conditions. Here we define our Reynolds number as $Re = cH_{av}/\nu$, which is five times larger than the corresponding Reynolds number, Re_{TP}, in [37]. The geometry of the channel is defined by the parameters $\alpha = 0.4$ and $L/H_{av} = 1$. The resolution of the computational mesh was 64 Fourier and 33 Chebyshev modes. The time step was 10^{-3} dimensionless units. We performed runs at $Re = 0.5$, 5, 50 ($Re_{TP} = 0.1$, 1, 10), with no pressure drop across the channel, to reproduce the results in Figs. 6, 12, 13 from [37] which we present in Figs. 8, 9, and 10. It can be seen that there is almost full quantitative agreement, the only minor differences being at a few points close to the boundary. It is reasonable to

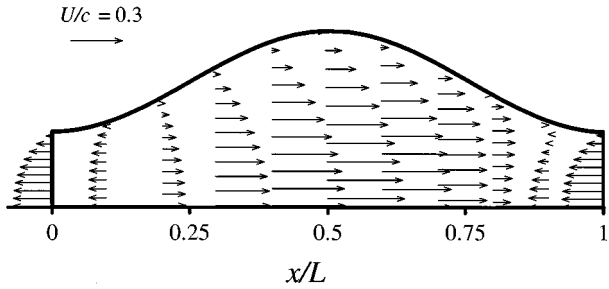

FIG. 9. Longitudinal velocity profiles for $Re = 5$, $\alpha = 0.4$, $L/H_{av} = 5$, and $\Delta P/\Delta L = 0$ in peristaltic flow calculated in the wave frame. The peristaltic wall (upper boundary) moves from left to right.

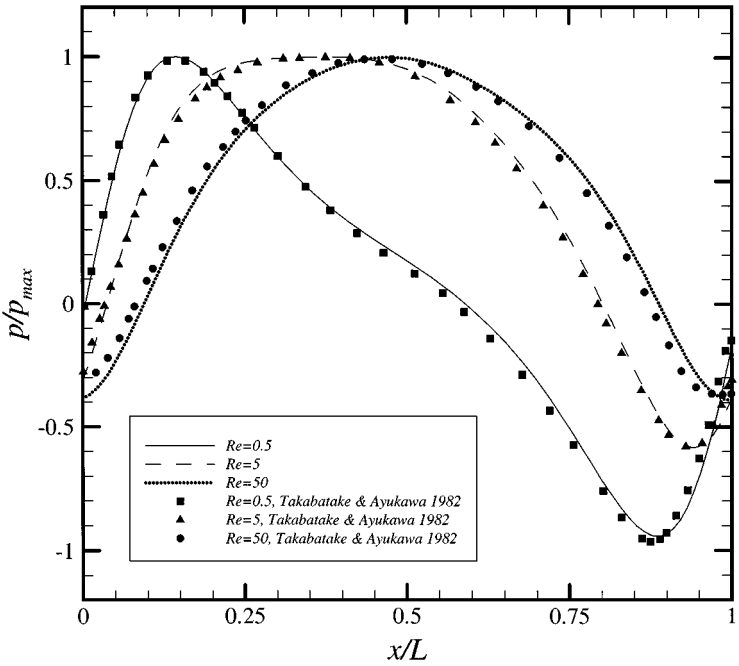

FIG. 10. Pressure distributions along the peristaltic wall for various Re and $\alpha = 0.4$, $L/H_{av} = 5$, and $\Delta P/\Delta L = 0$ in peristaltic flow calculated in the wave frame. The peristaltic wall (upper boundary) moves from left to right.

assume that our higher-order spectral method is more accurate than the finite-difference scheme in [37].

After the method was validated in the wave frame the final step was to validate it in the laboratory frame. Here we used Eqs. (42) and (44). In addition, we used the mapping to obtain only the derivatives of the coordinates x, y. The values of x, y were calculated through explicit second-order Adams–Bashforth integration. We could also have used a more accurate scheme like Runge–Kutta, since in this case the integration of the derivatives of the coordinates does not affect the time-discretization of the Navier–Stokes equations. There were two issues to examine. The first issue was to see whether the laboratory frame integration of the solution in the wave frame is stable (Run A). Secondly, we wanted to see if the method will converge to the correct solution starting from a different initial velocity field (Run B). We chose to perform a run at $Re = 1$, $\alpha = 0.1$, $L/H_{av} = 56/13$, and $\Delta t = 10^{-3}$ in this case. We chose a smaller amplitude in order to have a more accurate solution of the mapping with the same mesh than before, so that we could see whether the difference in the solutions is dominated by the integration of the coordinates and we get a method exhibiting second-order accuracy in time. The smaller Re resulted in smaller integration times. In Fig. 11 we have plotted the flowrate in time obtained from these two runs. The negative value is because we have a net flow from right to left. It is evident that they converge nicely on each other and that both are stable. Depending on time step used (10^{-3} and 10^{-4}), we obtained agreement to 6 and 8 digits, respectively, with the wave frame solution, for which we know exactly the values of x, y. This implies that the accuracy with which we know the coordinates dominates the error in the method. This is natural, since we have used extensively identities of the orthogonality of the mapping. However, since this is an

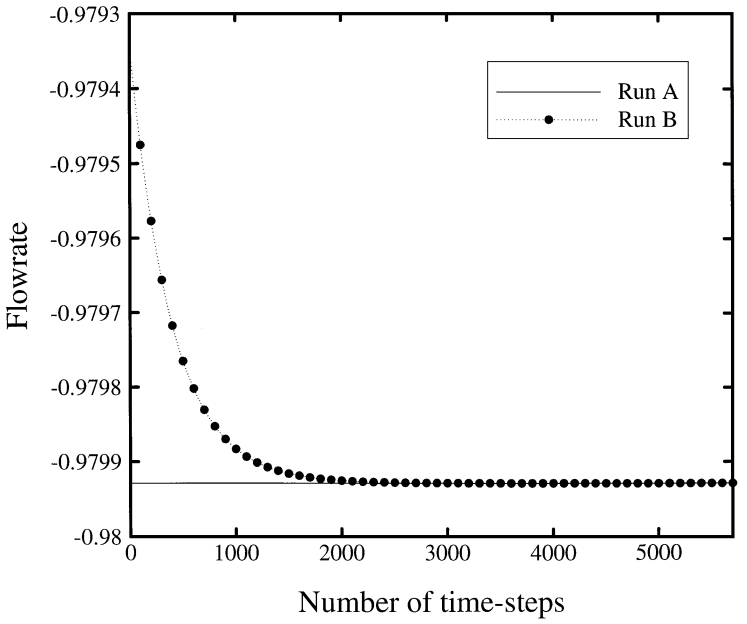

FIG. 11. Demonstration of convergence (Run B) and stability (Run A) of the algorithm in the laboratory frame, for peristaltic flow with $Re = 1$, $\alpha = 0.1$, $L/H_{av} = 56/13$, and $\Delta P/\Delta L = 0$. The peristaltic wall (upper boundary) moves from left to right.

efficient $O(N \log_2 N)$ technique, we can afford to go to larger meshes and solve problems with large surface deformations and higher Reynolds numbers more easily than most other numerical schemes.

5. CONCLUSIONS

We have developed and verified a numerical scheme for solving spectrally two-dimensional, time-dependent flow problems in moderately complex geometries. This method exhibits almost linear scalability and exponential convergence. It uses an orthogonal mapping algorithm, an efficient and robust iterative solver, and the influence matrix method for satisfying the incompressibility condition. It is easily extendible to three-dimensional and/or free-surface flows with or without surfactants. In addition, the algorithm can be parallelized in a straightforward fashion. Thus, it provides a unique new computational tool for the calculation of complex multi-dimensional and time-dependent flows.

APPENDIX A: PSEUDOCONFORMAL CURVILINEAR COORDINATE SYSTEM

In this appendix, the expressions of the various terms entering the model equations are presented for a generalized orthogonal curvilinear and time-dependent coordinate system. The notation used follows the conventions in [63] as far as both operators (gradient, covariant derivative, divergence, Laplacian, curl, *etc*.) and vector components. For an arbitrary vector, **c**, its covariant components are respesented by lowered indices c_i and its contravariant components by raised indices c^i, where i is an arbitrary dummy index. When necessary, the Einstein summation convention for repeated indices is utilized.

Finally, the coordinates ξ, η are, in general, denoted by u^i, where $i = 1, 2$ is a dummy index.

For the covariant component of the time derivative of the velocity $\mathbf{v}$, we take its inner product with the covariant basis vector $\mathbf{g}_i$,

$$\mathbf{g}_i \cdot \frac{\partial \mathbf{v}}{\partial t}\bigg|_{x(t),y(t)} = \frac{\partial v_i}{\partial t}\bigg|_{u^j} + \left[\frac{\partial v_i}{\partial u^j} - v_k \Gamma^k_{ij}\right]\frac{du^j}{dt} - v_k \mathbf{g}^k \cdot \frac{\partial \mathbf{g}_i}{\partial t}\bigg|_{u^j}, \tag{47}$$

where Γ^k_{ij} represents a Christoffel symbol for the curvilinear coordinate system and $\mathbf{g}^k$ the contravariant basis vector. The last two terms on the right-hand side are present only when the coordinate system exhibits a time dependence, as in the case of a moving and deforming boundary, and are treated, as mentioned before, explicitly in the time integration scheme exactly like the nonlinear convective terms for the velocity in the Navier–Stokes equation. When the coordinate system does not change, such as for a stationary or uniformly translating boundary, these last two terms drop out.

The components along ξ of the middle term in Eq. (47) are

$$\begin{aligned}\left[\frac{\partial v_\xi}{\partial u^j} - v_k \Gamma^k_{\xi j}\right]\frac{du^j}{dt} &= \left[\frac{\partial v_\xi}{\partial \xi} - \frac{\partial \ln h_\xi}{\partial \xi} v_\xi - M\frac{\partial \ln h_\xi}{\partial \eta} v_\eta\right]\frac{d\xi}{dt} \\ &\quad + \left[\frac{\partial v_\xi}{\partial \eta} - \frac{\partial \ln h_\xi}{\partial \eta} v_\xi - M\frac{\partial \ln h_\xi}{\partial \xi} v_\eta\right]\frac{d\eta}{dt}, \end{aligned} \tag{48}$$

$$\begin{aligned}\left[\frac{\partial v_\eta}{\partial u^j} - v_k \Gamma^k_{\eta j}\right]\frac{du^j}{dt} &= \left[\frac{\partial v_\eta}{\partial \xi} - \frac{\partial \ln h_\xi}{\partial \eta} v_\xi - \frac{\partial \ln h_\xi}{\partial \xi} v_\eta\right]\frac{d\xi}{dt} \\ &\quad + \left[\frac{\partial v_\eta}{\partial \eta} + \frac{1}{M}\frac{\partial \ln h_\xi}{\partial \xi} v_\xi - \frac{\partial \ln h_\xi}{\partial \eta} v_\eta\right]\frac{d\eta}{dt}. \end{aligned} \tag{49}$$

For the last term in (47) we have

$$v_k \mathbf{g}^k \cdot \frac{\partial \mathbf{g}_\xi}{\partial t}\bigg|_\eta = \left[v_\xi\left(g^\xi_x \mathbf{e}_x + g^\xi_y \mathbf{e}_y\right) + v_\eta\left(g^\eta_x \mathbf{e}_x + g^\eta_y \mathbf{e}_y\right)\right] \cdot \left[\frac{\partial}{\partial \xi}\left(\frac{\partial x}{\partial t}\right)\mathbf{e}_x + \frac{\partial}{\partial \xi}\left(\frac{\partial y}{\partial t}\right)\mathbf{e}_y\right] \tag{50}$$

and

$$v_k \mathbf{g}^k \cdot \frac{\partial \mathbf{g}_\eta}{\partial t}\bigg|_\xi = \left[v_\xi\left(g^\xi_x \mathbf{e}_x + g^\xi_y \mathbf{e}_y\right) + v_\eta\left(g^\eta_x \mathbf{e}_x + g^\eta_y \mathbf{e}_y\right)\right] \cdot \left[\frac{\partial}{\partial \eta}\left(\frac{\partial x}{\partial t}\right)\mathbf{e}_x + \frac{\partial}{\partial \eta}\left(\frac{\partial y}{\partial t}\right)\mathbf{e}_y\right], \tag{51}$$

where $\mathbf{e}_x$ and $\mathbf{e}_y$ are the Cartesian basis vectors for a two dimensional coordinate system and g^ξ_x, g^ξ_y and g^η_x, g^η_y the components of the contravariant basis vectors in the Cartesian frame.

The covariant components of the Laplacian of the velocity which enter into the equations of motion are

$$(\nabla^2 \mathbf{v})_\xi = \frac{1}{h^2_\xi}\frac{\partial^2 v_\xi}{\partial \xi^2} + \frac{1}{h^2_\eta}\frac{\partial^2 v_\xi}{\partial \eta^2} - 2\frac{M}{h^2_\xi}\left(\frac{\partial v_\xi}{\partial \eta} - \frac{\partial v_\eta}{\partial \xi}\right)\frac{\partial \ln h_\xi}{\partial \eta} - \frac{1}{h^2_\xi} v_\xi\left(\frac{\partial^2 \ln h_\xi}{\partial \xi^2} + M\frac{\partial^2 \ln h_\xi}{\partial \eta^2}\right). \tag{52}$$

and

$$(\nabla^2\mathbf{v})_\eta = \frac{1}{h_\xi^2}\frac{\partial^2 v_\eta}{\partial\xi^2} + \frac{1}{h_\eta^2}\frac{\partial^2 v_\xi}{\partial\eta^2} + \frac{2}{h_\xi^2}\left(\frac{\partial v_\xi}{\partial\eta} - \frac{\partial v_\eta}{\partial\xi}\right)\frac{\partial \ln h_\xi}{\partial\xi} - \frac{1}{h_\xi^2}v_\eta\left(\frac{\partial^2 \ln h_\xi}{\partial\xi^2} + M\frac{\partial^2 \ln h_\xi}{\partial\eta^2}\right). \tag{53}$$

The scaled value of the divergence of the Laplacian of the velocity for an incompressible fluid, which is used in the derivation of the Poisson equation for the pressure, is taken from the formula

$$\begin{aligned}\left(\frac{M}{h_\xi^2}\right)&\boldsymbol{\nabla}\cdot\nabla^2\mathbf{v}\\ &\equiv \frac{1}{M}\frac{\partial}{\partial\xi}(\boldsymbol{\nabla}\cdot\boldsymbol{\nabla}\mathbf{v})_\xi + \frac{\partial}{\partial\eta}(\boldsymbol{\nabla}\cdot\boldsymbol{\nabla}\mathbf{v})_\eta\\ &= \left(\frac{1}{h_\xi^2}\right)\left(\frac{1}{M}\frac{\partial^2 \ln h_\xi}{\partial\xi^2} + \frac{\partial^2 \ln h_\xi}{\partial\eta^2}\right)\left[2\left(v_\xi\frac{\partial \ln h_\xi}{\partial\xi} + Mv_\eta\frac{\partial \ln h_\xi}{\partial\eta}\right) - \frac{v_\xi}{M} - v_\eta\right].\end{aligned} \tag{54}$$

Finally, the covariant components of the rotational part of the convective terms in the equations of motion along ξ and η are

$$(\boldsymbol{\omega}\times\mathbf{v})_\xi = \frac{1}{h_\eta^2}\left(\frac{\partial v_\xi}{\partial\eta} - \frac{\partial v_\eta}{\partial\xi}\right)v_\eta \tag{55}$$

$$(\boldsymbol{\omega}\times\mathbf{v})_\eta = \frac{1}{h_\xi^2}\left(\frac{\partial v_\eta}{\partial\xi} - \frac{\partial v_\xi}{\partial\eta}\right)v_\xi. \tag{56}$$

APPENDIX B: DEFINITION OF THE RIGHT HAND SIDES OF THE DISCRETIZED MOMENTUM AND PRESSURE EQUATIONS

$$[\mathrm{RHS}(\mathbf{v};\, t = t_{n+1})]_\xi \equiv 2\left[\left(\frac{\partial v_\xi}{\partial\eta} - \frac{\partial v_\eta}{\partial\xi}\right)\frac{\partial \ln h_\xi}{\partial\eta}\right]^{n+1} + \left[v_\xi\left(\frac{1}{M}\frac{\partial^2 \ln h_\xi}{\partial\xi^2} + \frac{\partial^2 \ln h_\xi}{\partial\eta^2}\right)\right]^{n+1} \tag{57}$$

$$[\mathrm{RHS}(\mathbf{v};\, t < t_{n+1})]_\xi \equiv \left(\frac{h_\xi^2}{M}\right)^{n+1}\left[-\frac{2Re}{\Delta t}\mathbf{v}^n - (\nabla^2\mathbf{v})^n\right]_\xi - Re\left(\frac{h_\xi^2}{M}\right)^{n+1}[(\boldsymbol{\omega}\times\mathbf{v})^{n-1} - 3(\boldsymbol{\omega}\times\mathbf{v})^n]_\xi \tag{58}$$

$$[\mathrm{RHS}(\mathbf{v};\, t = t_{n+1})]_\eta \equiv -\left[\frac{2}{M}\left(\frac{\partial v_\xi}{\partial\eta} - \frac{\partial v_\eta}{\partial\xi}\right)\frac{\partial \ln h_\xi}{\partial\xi}\right]^{n+1} + \left[v_\eta\left(\frac{1}{M}\frac{\partial^2 \ln h_\xi}{\partial\xi^2} + \frac{\partial^2 \ln h_\xi}{\partial\eta^2}\right)\right]^{n+1} \tag{59}$$

$$[\mathrm{RHS}(\mathbf{v};\, t < t_{n+1})]_\eta \equiv \left(\frac{h_\xi^2}{M}\right)^{n+1}\left[-\frac{2Re}{\Delta t}\mathbf{v}^n - (\nabla^2\mathbf{v})^n\right]_\eta - Re\left(\frac{h_\xi^2}{M}\right)^{n+1}[(\boldsymbol{\omega}\times\mathbf{v})^{n-1} - 3(\boldsymbol{\omega}\times\mathbf{v})^n]_\eta \tag{60}$$

$$\mathrm{RHS}(p; t = t_{n+1}) \equiv \frac{1}{2Re}\left(\frac{1}{h_\xi^2}\right)^{n+1}\left(\frac{1}{M}\frac{\partial^2 \ln h_\xi}{\partial \xi^2} + \frac{\partial^2 \ln h_\xi}{\partial \eta^2}\right)^{n+1} \times \left[2\left(v_\xi \frac{\partial \ln h_\xi}{\partial \xi} + M v_\eta \frac{\partial \ln h_\xi}{\partial \eta}\right) - \frac{v_\xi}{M} - v_\eta\right]^{n+1} \tag{61}$$

$$\mathrm{RHS}(p; t < t_{n+1}) \equiv \left(\frac{h_\xi^2}{M}\right)^{n+1}\left\{\frac{1}{2}\boldsymbol{\nabla}^{n+1} \cdot [(\boldsymbol{\omega} \times \mathbf{v})^{n-1} - 3(\boldsymbol{\omega} \times \mathbf{v})^n] - \frac{1}{2Re}\boldsymbol{\nabla}^{n+1} \cdot \left[-\frac{2Re}{\Delta t}\mathbf{v}^n - (\nabla^2 \mathbf{v})^n\right]\right\}. \tag{62}$$

ACKNOWLEDGMENTS

The authors acknowledge gratefully the financial support provided by the Office of Naval Research under Grant N00014-94-1-0581. The use of the computational facilities at the University of Delaware to perform part of the required calculations, specifically the Cray Research J916/8 and the two IBM RS6000/990 systems, is also acknowledged.

REFERENCES

1. T. F. Swean, Jr., and A. N. Beris, Dynamics of free surface flows with surfactants, *Appl. Mech. Rev.* **47**, S173 (1994).
2. T. Sarpkaya, Vorticity, free-surface, and surfactants, *Ann. Rev. Fluid Mech.* **28**, 83 (1996).
3. C. Canuto, M. Y. Hussaini, A. Quarteroni, and T. A. Zang, *Spectral Methods in Fluid Dynamics* (Springer-Verlag, Berlin, 1992), 2nd ed.
4. S. A. Orszag, M. Israeli, and M. O. Deville, Boundary conditions for incompressible flows, *J. Sci. Comput.* **1**, 75 (1986).
5. S. A. Orszag and G. S. Patterson, Jr., Numerical simulation of three-dimensional homogeneous isotropic turbulence, *Phys. Rev. Lett.* **28**, 76 (1972).
6. S. A. Orszag and L. C. Kells, Transition to turbulence in plane Poiseuille and plane Couette flow, *J. Fluid Mech.* **96**, 159 (1980).
7. D. Gottlieb, M. Y. Hussaini, and S. A. Orszag, *Spectral Methods for Partial Differential Equations*, edited by R. G. Voigt, D. Gottlieb, and M. Y. Hussaini (SIAM, Philadelphia, 1984).
8. W. T. Tsai and D. K. P. Yue, Computation of nonlinear free-surface flows, *Ann. Rev. Fluid Mech.* **28**, 249 (1996).
9. K. N. Christodoulou and L. E. Scriven, The fluid mechanics of slide coating, *J. Fluid. Mech.* **208**, 321 (1989).
10. R. Glowinski and O. Pironneau, Finite element methods for Navier–Stokes equations, *Ann. Rev. Fluid Mech.* **24**, 167 (1992).
11. J. U. Brackbill, D. B. Kothe, and C. Zemach, A continuum method for modeling surface tension, *J. Comput. Phys.* **100**, 335 (1992).
12. E. G. Puckett, A. S. Almgren, J. B. Bell, D. L. Marcus, and W. J. Rider, A high-order projection method for tracking fluid interfaces in variable density incompressible flows, *J. Comput. Phys.* **130**, 269 (1997).
13. S. A. Orszag, Spectral methods for problems in complex geometries, *J. Comput. Phys.* **37**, 70 (1980).
14. A. T. Patera, A spectral element method for fluid dynamics: Laminar flow in a channel expansion, *J. Comput. Phys.* **54**, 468 (1984).
15. G. E. Karniadakis, E. T. Bullister, and A. T. Patera, A spectral element method for solution of the two- and three-dimensional time-dependent incompressible Navier–Stokes equations, in *Proc. Europe-U.S. Conf. Finite Element Methods for Nonlinear Problems*, edited by P. Bergan and K. J. Bathe (Springer-Verlag, Berlin, 1985), p. 803.

16. A. Farcy and T. A. de Roquefort, Chebyshev pseudospectral solution of the incompressible Navier–Stokes equations in curvilinear domains, *Comput. Fluids* **16**, 459 (1988).
17. C. D. Dimitropoulos and A. N. Beris, An efficient and robust spectral solver for nonseparable elliptic equations, *J. Comput. Phys.* **133**, 186 (1997).
18. J. F. Thompson, Z. U. A. Warsi, and C. W. Mastin, *Numerical Grid Generation: Foundations and Applications*. (North-Holland, New York, 1985).
19. J. F. Thompson, Z. U. A. Warsi, and C. W. Mastin, Boundary-fitted coordinate systems for numerical solution of partial differential equations, *J. Comput. Phys.* **47**, 1 (1982).
20. Z. U. A. Warsi, Note on the mathematical formulation of the problem of numerical coordinate generation, *Quart. Appl. Math.* **41**, 221 (1983).
21. C. D. Mobley and R. J. Stewart, On the numerical generation of boundary-fitted orthogonal curvilinear coordinate systems, *J. Comput. Phys.* **34**, 124 (1980).
22. B. Fornberg, A numerical method for conformal mappings, *SIAM J. Sci. Stat. Comput.* **1**, 386 (1980).
23. G. Ryskin and L. G. Leal, Orthogonal mapping, *J. Comput. Phys.* **50**, 71 (1983).
24. I. S. Kang and L. G. Leal, Orthogonal grid generation in a 2D domain via the boundary integral technique, *J. Comput. Phys.* **102**, 78 (1992).
25. R. Duraiswami and A. Prosperetti, Orthogonal mapping in two dimensions, *J. Comput. Phys.* **98**, 254 (1992).
26. I. J. Sobey, On flow through furrowed channels. Part 1. Calculated flow patterns, *J. Fluid Mech.* **96**, 1 (1980).
27. I. J. Sobey, Occurrence of separation in oscillatory flow, *J. Fluid Mech.* **134**, 247 (1983).
28. I. J. Sobey, Observation of waves during oscillatory channel flow, *J. Fluid Mech.* **151**, 395 (1985).
29. C. Pozrikidis, Creeping flow in two-dimensional channels, *J. Fluid. Mech.* **180**, 495 (1987).
30. T. Nishimura, Y. Ohori, and Y. Kawamura, Flow characteristics in a channel with symmetric wavy wall for steady flow, *J. Chem. Eng. Japan* **17**, 466 (1984).
31. T. Nishimura, T. Yoshino, and Y. Kawamura, Numerical flow analysis of pulsatile flow in a channel with symmetric wavy walls at moderate Reynolds number, *J. Chem. Eng. Japan* **20**, 479 (1987).
32. T. Nishimura, S. Murakami, S. Arakawa, and Y. Kawamura, Flow observations and mass transfer characteristics in symmetrical wavy-walled channels at moderate Reynolds numbers for steady flow, *Int. J. Heat Mass Transfer* **33**, 835 (1990).
33. T. Nishimura, S. Arakawa, S. Murakami, and Y. Kawamura, Oscillatory viscous flow in symmetric wavy-walled channels, *Chem. Eng. Sci.* **44**, 2137 (1989).
34. T. Nishimura, H. Miyashita, S.Murakami, and Y. Kawamura, Oscillatory flow in a symmetric sinusoidal wavy-walled channel at intermediate Strouhal numbers, *Chem. Eng. Sci.* **46**, 757 (1991).
35. J. C. Burns and T. Parkes, Peristaltic motion, *J. Fluid Mech.* **29**, 731 (1967).
36. C. Pozrikidis, A study of peristaltic flow, *J. Fluid. Mech.* **180**, 515 (1987).
37. S. Takabatake and K. Ayukawa, Numerical study of two-dimensional peristaltic flows, *J. Fluid Mech.* **122**, 439 (1982).
38. B. V. R. Kumar and K. B. Naidu, A numerical study of peristaltic flows, *Comput. Fluids* **24**, 161 (1995).
39. S. Takabatake, K. Ayukawa, and A. Mori, Persitaltic pumping in circular cylindrical tubes: A numerical study of fluid transport and its efficiency, *J. Fluid Mech.* **193**, 267 (1988).
40. G. Boehme and R. Friedrich, Peristaltic flow of viscoelastic liquids, *J. Fluid Mech.* **128**, 109 (1983).
41. A. Karageorghis and T. N. Phillips, Conforming Chebyshev collocation methods for the solution of laminar flow in a constricted channel, *IMA J. Numer. Anal.* **11**, 33 (1991).
42. L.-W. Ho and A. T. Patera, Legendre spectral element method for simulation of unsteady incompressible viscous free-surface flows, *Comput. Methods Appl. Mech. Eng.* **80**, 355 (1990).
43. L. Kleiser and U. Schumann, Treatment of incompressibility and boundary conditions in 3-D numerical spectral simulations of plane channel flow, in *Proc. 3rd GAMM Conference on Numerical Methods in Fluid Mechanics*, edited by E. H. Herschel (Vieweg-Verlag, Braunschweig, 1980), p. 165.
44. T. N. Phillips and I. M. Soliman, Influence matrix technique for the numerical spectral simulation of viscous incompressible flows, *Numer. Methods Partial Differential Equations* **7**, 9 (1991).

45. P. M. Gresho and R. L. Sani, On pressure boundary conditions for the incompressible Navier–Stokes equations, *Int. J. Numer. Methods Fluids* **7**, 1111 (1987).
46. P. M. Gresho, Some current CFD issues relevant to incompressible Navier–Stokes equations, *Comput. Methods Appl. Mech. Eng.* **87**, 201 (1991).
47. P. Moin and J. Kim, On the numerical solution of time-dependent viscous incompressible fluid flows involving solid boundaries, *J. Comput. Phys.* **35**, 381 (1980).
48. J. Kim and P. Moin, Application of a fractional-step method to incompressible Navier–Stokes equations, *J. Comput. Phys.* **59**, 308 (1985).
49. E. W. Miner, T. F. Swean, Jr., R. A. Handler, and R. I. Leighton, Examination of wall damping for the k-ϵ turbulence model using direct numerical simulations of turbulent channel flow, *Int. J. Numer. Methods Fluids* **12**, 609 (1991).
50. K. S. Ball, R. A. Handler, and L. Sirovich, Dynamics of coherent structures in wall bounded turbulence, in *Research Trends in Physics: Chaotic Dynamics and Transport in Fluids and Plasmas*, edited by W. Horton, Y. Ichikawa, I. Prigogine, and G. Zaslavsky (La Jolla International School of Physics, La Jolla, CA, 1992), p. 149.
51. A. N. Beris and R. Sureshkumar, Simulation of time-dependent viscoelastic channel Poiseuille flow at high Reynolds numbers, *Chem. Eng. Sci.* **51**, 1451 (1996).
52. R. Sureshkumar, A. N. Beris, and R. A. Handler, Direct numerical simulation of turbulent channel flow of a dilute polymer solution, *Phys. Fluids* **9**, 743 (1997).
53. C. Canuto and A. Quarteroni, Preconditioned minimal residual methods for Chebyshev spectral calculations, *J. Comput. Phys.* **60**, 315 (1985).
54. T. A. Zang, Y. S. Wong, and M. Y. Hussaini, Spectral multigrid methods for elliptic equations, *J. Comput. Phys.* **48**, 485 (1982).
55. T. A. Zang, Y. S. Wong, and M. Y. Hussaini, Spectral multigrid methods for elliptic equations, II, *J. Comput. Phys.* **54**, 489 (1984).
56. J. S. Hesthaven, Integration preconditioning of pseudospectral operators. I. Basic linear operators, *SIAM J. Numer. Anal.* **35**, 1571 (1998).
57. G. L. G. Sleijpen and D. R. Fokkema, BiCGstab(l) for linear equations involving unsymmetric matrices with complex spectrum, *Electron. Trans. Numer. Anal.* **1**, 11 (1993).
58. H. A. Van der Vorst, Bi-CGSTAB: A fast and smoothly converging variant of Bi-CG for the solution of nonsymmetric linear systems, *SIAM J. Sci. Stat. Comput.* **13**(2), 631 (1992).
59. P. Concus and G. H. Golub, Use of fast direct methods for the efficient numerical solution of non-separable elliptic equations, *SIAM J. Numer. Anal.* **10**(6), 1103 (1973).
60. A. N. Beris, M. Avgousti, and A. Souvaliotis, Spectral calculations of viscoelastic flows: Evaluation of the Giesekus constitutive equation in model flow geometries, *J. Non-Newtonian Fluid Mech.* **44**, 197 (1992).
61. A. Souvaliotis and A. N. Beris, Spectral collocation/domain decomposition method for viscoelastic flow simulations in model porous geometries, *Comput. Methods Appl. Mech. Eng.* **129**, 9 (1996).
62. A. Souvaliotis, *Steady-State Polymeric Flow in Model Porous Media*, Ph.D. Thesis, University of Delaware, 1993.
63. J. G. Simmonds, *A Brief on Tensor Analysis* (Springer-Verlag, Berlin, 1994), 2nd ed.